WILEY-VCH

DOI: 10.1002/adom.201600296
Article type: Full Paper

Upconversion Nanocrystals Doped Glass: A New Paradigm for Photonic Materials

Jiangbo Zhao[1,4], Xianlin Zheng[2,4], Erik P. Schartner[1,4], Paul Ionescu[3], Run Zhang[1], Tich-Lam Nguyen[3], Dayong Jin[2,4,5], Heike Ebendorff-Heidepriem[1,4*]*

[1]Institute for Photonics and Advanced Sensing and School of Physical Sciences, University of Adelaide, Adelaide, SA 5005, Australia

[2]Advanced Cytometry Laboratories, MQ Biofocus Research Centre, Macquarie University, Sydney, NSW 2109, Australia

[3]Bio21 Institute and School of Chemistry, University of Melbourne, Melbourne, VIC 3010, Australia

[4]ARC Centre of Excellence for Nanoscale BioPhotonics

[5]Institute for Biomedical Materials and Devices, Faculty of Science, University of Technology Sydney, NSW, 2007, Australia

Abstract

The integration of novel luminescent nanomaterials into glassy matrix can lead to new hybrid materials and photonic devices with promising material performance and device functions. Lanthanide-containing upconversion nanocrystals have become promising candidates for sensing, bio-imaging, photon energy management, volumetric displays, and other photonic applications. Here, we develop a versatile direct-doping approach to integrate bright upconversion nanocrystals, with tailored nanoscale properties in tellurite glass. Following our two-temperature glass-melting technique, we determine the doping temperature window of 550-625 ºC, with a 5 min dwell time at 577 ºC are the key to success, by balancing the survival and dispersion of upconversion nanocrystals in glass. We identify that the fine spectra of upconversion emissions can be used to diagnose the survival and dissolution fraction of doped nanocrystals in the glass. Moreover, we visualize three-dimensional dispersion of nanocrystals in the glass by upconversion scanning confocal microscopy. We further demonstrate that a low-loss fiber, drawn from the highly transparent nanocrystals-doped glass retains the unique optical properties of upconversion nanocrystals. These results suggest a robust strategy for fabrication of high quality upconversion nanocrystals-doped glasses. The new class of hybrid glasses allow for fiber-based devices to be developed for photonic applications or as a useful tool for tailoring light–nanoparticles interactions study.

Keywords: upconversion, lanthanide, spectroscopy, photonic material, glass fiber

1. Introduction

Upconversion nanocrystals (UPNCs) contain thousands of trivalent lanthanide ions (Ln^{3+}) forming an efficient network of photon-sensitizers, energy migration transducers, and photon emitters. This Ln^{3+} ions network enables higher-energy emissions in the ultraviolet to visible spectral range by up-converting two or more near-infrared excitation photons. UPNCs with high concentrations of active Ln^{3+} ions have been recently discovered to emit high brightness upconversion by utilizing high-irradiance excitation [1], or clustering Yb^{3+} sensitizers in arrays at sublattice level to promote localized excited states [2]. Many novel photonics properties at the nanoscale, including colour tuning, time-domain response and energy migration of upconversion emissions, have also been realized by precisely engineering the core-shell structure [3] or morphology [4] of UPNCs. The new-generation UPNCs have generated strong interest for various applications [5], such as biological sensing, biomedical imaging, anti-counterfeiting, data storage, solar energy management, and 3D volumetric displays.

In addition to the bio/nano-photonics applications of high-brightness UPNCs, there has been growing attraction to integrate UPNCs with a photonic platform to harness their outstanding nanoscale properties in photonic devices [6] and provide a previously unexplored avenue to study light–nanoparticle interactions. Glass is an indispensable photonic platform material due to its high optical transparency, thermomechanical strength and the ability to be shaped into an almost unlimited range of geometrical structures. However, it remains challenging to integrate UPNCs with tailored nanophotonic properties in a glassy matrix to create a new hybrid photonic material.

To date, the almost exclusively used approach to integrate Ln^{3+}-containing nanocrystals (NCs) in glass is the so-called glass ceramics method, which relies on the *in-situ* growth of NCs in a glass matrix [7]. In this method, the glass containing precursor ions is heated above the glass transition temperature to facilitate diffusion of ions inside the glass to form crystal seeds that grow into *in-situ* NCs [7b, 8] (Figure 1a and 1b). Whilst the conventional glass ceramics method has achieved remarkable progress in embedding NCs in glass [9], it remains challenging to attain a high level of compositional and nanostructural control of Ln^{3+}-containing NCs grown *in-situ* in a glass. Firstly, the glass ceramics method poses intrinsic limitations on the incorporation of Ln^{3+} ions in *in-situ* grown NCs in well-defined concentrations and with controlled arrangement at specific crystalline sites. In addition, the combination of restricted solubility of Ln^{3+} ions [10] and their short-distance diffusion in glass [11], as well as the large volume fractions of 25-35% of *in-situ* grown NCs (NCs/glass vol/vol) [12] limits the maximum Ln^{3+} concentration that can be obtained in these NCs (Figure 1b and 1d). Secondly, growing core-shell and heterogeneous nanostructures in Ln^{3+}-containing NCs to engineer optical properties at a nanoscale is not possible *via* the glass ceramics method [13]. Thirdly, the application of glass ceramics is hampered by continued growth of *in-situ* grown NCs which could occur during a post-annealing or reheating process such as fiber drawing [14]. The continued growth of NCs leads to increased light scattering and high optical loss in the resulting glass/fiber.

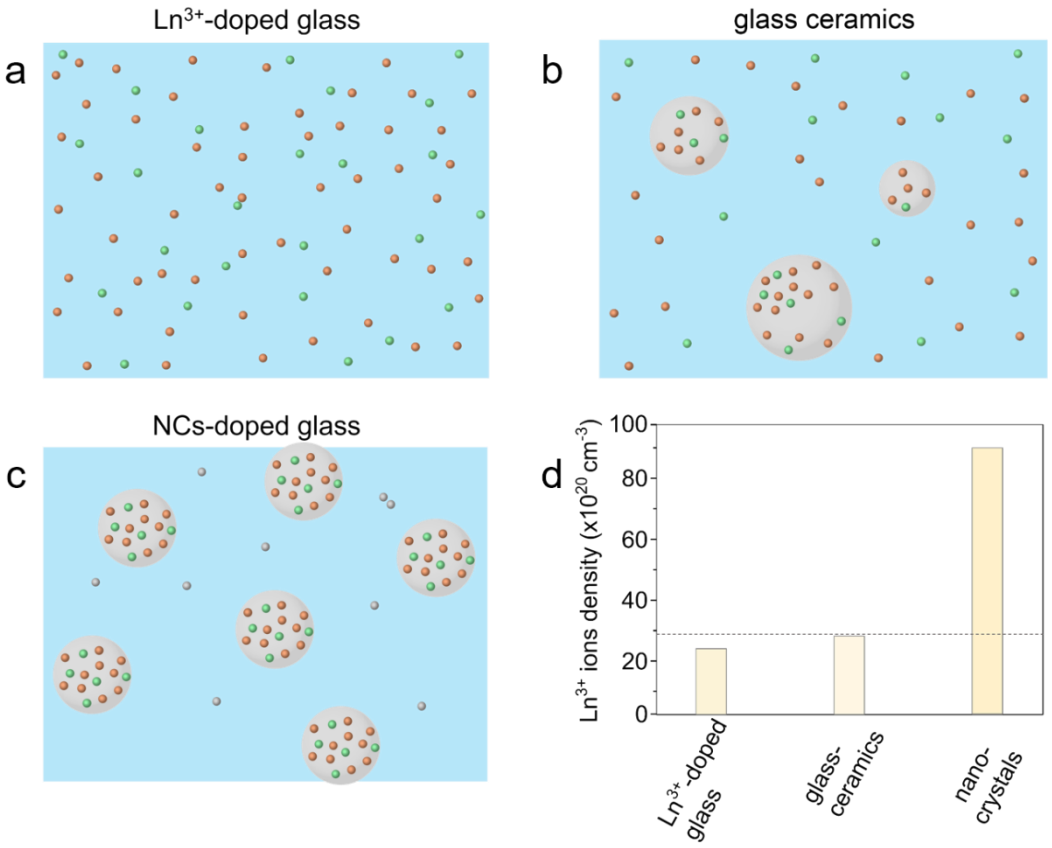

Figure 1. Schematic diagram of Ln^{3+} distribution in various glasses. a, glass containing Ln^{3+} ions (Ln^{3+}-doped glass), **b,** glass containing *in-situ* grown NCs (glass ceramics), **c,** glass with directly doped NCs (NCs-doped glass). The small grey dots represent the Ln^{3+} ions in NCs-doped glass that were formed by dissolution of NCs, which could be prevented by using NCs with a robust shell. **d**, Schematic of Ln^{3+} ion densities available in glasses, NCs in glass ceramics, and as-synthesized individual NCs, indicating that up to 23×10^{20} Ln^{3+}/cm^3, and 28×10^{20} Ln^{3+}/cm^3 have been achieved in glasses and glass ceramics respectively, whereas up to 90×10^{20} Ln^{3+}/cm^3 is feasible in individual NCs synthesized in solvents. It is reported that up to ~10×10^{20} Ln^{3+}/cm^3 was doped in tellurite glass or ZBLAN glass [15], and up to 23×10^{20} Ln^{3+} ions/cm^3 was achieved in germanate glass [16]. The Ln^{3+} ions density of *in-situ* grown NCs in glass ceramics is slightly higher than that of Ln^{3+}-doped glass, since the Ln^{3+} ions in the glass are diffused and concentrated in the grown NCs. However, the relatively small diffusion of Ln^{3+} ions into the grown NCs (considerable residual Ln^{3+} in the glass matrix), and large volume fractions of these NCs in glass limit the maximum concentration of Ln^{3+} ions in grown

NCs. For instance, a doping level of 28×10^{20} Ln^{3+}/cm^3 was obtained when 30% of the total Ln^{3+} ions diffuse from the glass into *in-situ* grown NCs [11c], and 25% volume fraction of the grown NCs (NCs/glass vol/vol) occupy the glass [12]. In contrast, wet chemistry synthesis of NCs, where the ionic radius of the cationic sites in crystalline matrix is close to that of Ln^{3+} ions, permits the cationic sites to be completely occupied by Ln^{3+} ions. This enables considerably higher Ln^{3+} ion densities in as-synthesized NCs [1a, 17], and hence in such NCs-doped glass.

The ever-advancing synthetic techniques of UPNCs using wet chemistry have shown exceptional control over crystallite phase, size, shape, composition and nanostructure [1a, 1b, 4]. This control gives a clear advantage over *in-situ* glass ceramics technique by synthesizing NCs and glass separately, and then integrating them into a hybrid material. This fabrication strategy can afford the entire compositional and nanostructural control of the as-synthesized NCs and as-fabricated glass, and overcome the limitations of the glass ceramics method. One approach to deploy such a strategy is to pre-mix the as-synthesized NCs with glass powder, and re-melt the mixture into a hybrid glass. But, as reported in previous attempts [18], the pre-mixing technique was found to result in significant dissolution of the nano/micro-scale crystals and decreased transmittance in the resulting glass [19]. For example, the crystal size was reduced from 18.3 μm to 14 μm with a re-melting temperature at 520 ºC for a duration of 10 min [19b]. This protocol thus presents an extremely high risk of completely dissolving the nanoscale crystals. Alternatively, our recent success in directly doping nanodiamonds into a tellurite-based glass melt [20] suggests that fine control of the doping temperature and dwell time allows unique NCs to be embedded and the quality of the glass to be preserved. Therefore, the direct doping method is a favourable approach to integrate Ln^{3+}-containing

UPNCs in glass, although the challenge remains to ensure the survival of UPNCs in the high temperature glass melt.

Here we demonstrate an UPNCs-doped glass created by directly doping as-synthesized NCs into tellurite-based glass as a novel hybrid photonic material (Figure 1c). The key to our success is the selection of the doping temperature in a temperature window of 550-625 ºC, and a 5 min dwell time to balance the survival and dispersion of the UPNCs in the glass melt. For the first time, we prove that this approach allows incorporation of a controlled amount of $LiYF_4$:Yb,Er UPNCs in glass with well-defined concentrations of Ln^{3+} ions. Our UPNCs-doped glasses show a high transparency and identical glass structure as blank tellurite glass (not doped with UPNCs). We also demonstrate that the fine structure of Er^{3+} emissions is suitable to distinguish glassy and crystalline environment of Er^{3+} ions. This allows for verification of the survival of doped Ln^{3+}-containing UPNCs, but also for the first time, quantitative investigation of their dissolution fraction in the glass. Furthermore, we illustrate a previously unrealized three-dimensional (3D) *in-situ* dispersion of UPNCs in the glass by upconversion scanning confocal microscopy. We draw the UPNCs-doped glass into an optical fiber with well-retained UPNCs and impressive low loss. All the results suggest a far more versatile and tailored approach for constructing a fiber-based photonic device using new NCs-doped glass.

2. Results and Discussion

For Ln^{3+}-containing UPNCs, the host lattice $LiYF_4$ was selected owing to its thermal stability, low crystallographic site symmetry (point group S_4 for coordinated Ln^{3+}), low phonon energy

(~566 cm^{-1}), and reduced crystal defects (almost identical ionic radii of Y^{3+} to other Ln^{3+} minimizing lattice mismatch defects). These features make the $LiYF_4$ lattice one of the most efficient nanomaterials for upconversion emissions [21]. Moreover, the current synthesis technique is available to precisely engineer composition, phase, size and shape of such fluoride NCs [22], making them suitable as representative Ln^{3+}-containing NCs embedded in a glass *via* the direct doping method. In our case, $LiYF_4$ NCs are bipyramidal with edge lengths of 66±1.8 nm × 64±2.3 nm (Figure S1).

Er^{3+} ions were specifically used as active dopants. Since the upconversion emissions of Er^{3+} ions are hypersensitive to the surroundings in comparison to Tm^{3+} optical transitions (Figure S2) [23]. Both the Er^{3+} green and red upconversion emissions (including the line shape and position) are distinctively different in glassy and crystalline matrix (Figure S2). This spectroscopic feature is in particular useful to distinguish the Er^{3+} ions in the nanocrystalline lattice from those diffused into the amorphous glass matrix, since the Er^{3+} ions in the glassy environment show an absence of fine-structure spectroscopic features which are observed for Er^{3+} ions in the crystalline host. This indicates that the hypersensitivity of Er^{3+} emissions can be used to examine the survival and dissolution fraction of $LiYF_4$ NCs in the glass.

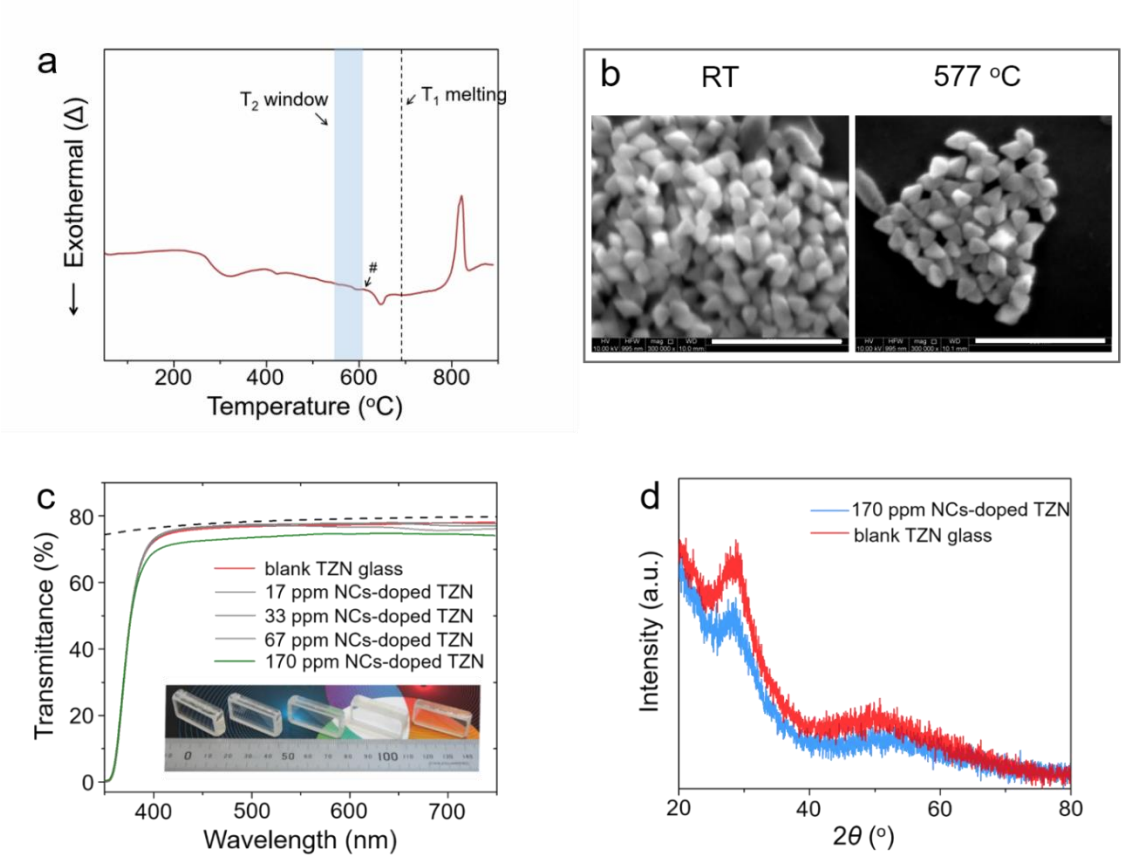

Figure 2. General characterizations of $LiYF_4$ NCs and NCs-doped TZN glasses. a, DTA analysis of $LiYF_4$ NCs to determine the decomposition temperature. The blue band represents the T_2 temperature window suitable for directly doping $LiYF_4$ NCs in TZN glass melt. The vertical dashed line is the batch melting temperature T_1 used for preparing TZN glass. The exothermic signal between 300 ºC and 450 ºC is ascribed to the oxidation of the original oleate ligands around $LiYF_4$ NCs. [24] **b,** SEM images of $LiYF_4$ NCs before (left column) and after (right column) annealing at 577 ºC for 5 min. $LiYF_4$ NCs was spiked on a glass coverslip for this test. Scale bar: 500 nm. **c,** Transmittance spectra of bulk TZN glasses doped with varying amounts of $LiYF_4$ NCs. The solid curves represent the averaged transmission spectra of three different spots of each glass and are normalized to a glass thickness of 5 mm as described in the supplement. The top dashed line is the calculated transmittance for TZN glass taking into account multiple Fresnel reflections at the sample surfaces as described in Figure S5 [25]. The exponential drop of the measured transmission results from the electronic band gap absorption of TZN glass. The bottom inset is an optical photograph of blank and NCs-doped TZN

glasses, left → right: blank TZN glass, ~ 17, 33, 67, and 170 ppm $LiYF_4$ NCs-doped TZN glasses. All samples are colourless and transparent. **d**. XRD spectra of blank and NCs-doped TZN glass, showing only the broad bands of amorphous glass and no crystalline footprint.

To succeed in directly doping $LiYF_4$ NCs into the glass, it is critical to identify a suitable glass melt temperature for doping and dispersing the $LiYF_4$:Yb,Er NCs in the glass melt. To survive doped NCs in the glass melt, the maximum doping temperature is limited by the decomposition temperature of $LiYF_4$ NCs. The decomposition temperature of $LiYF_4$ NCs was measured using Differential Thermal Analysis (DTA): two eutectic melting peaks at 647 ºC (minor) and 821 ºC (sharp and major) correspond to the decomposition of tetragonal $LiYF_4$ NCs [26]. Hence, the onset of the decomposition temperature (~625 ºC, symbol # in Figure 2a) of $LiYF_4$ NCs naturally constitutes the upper limit of the glass melt temperature that can be used for direct doping. Scanning electron microscopy (SEM) images (Figure 2b) and X-ray diffraction (XRD) pattern (Figure S3) of as-deposited and annealed $LiYF_4$ NCs (at 577 ºC) prove the stability of $LiYF_4$ NCs below the decomposition temperature.

The lower limit of the doping temperature is determined by the glass melt viscosity. As the glass melt viscosity increases with decreasing temperature, a temperature point exists where the glass melt is too viscous to disperse doped NCs in the melt. In our work, we selected the ternary tellurite glass TeO_2-ZnO-Na_2O with molar ratios of 75:15:10, hereafter referred to as TZN, as the glass matrix [25b]. The viscosity of TZN glass at 550 ºC is approximately 5 Pa·s (like honey at room temperature) [27], suggesting the lower doping temperature limit for TZN glass. Together with the maximum doping temperature given by the NCs decomposition temperature, the doping temperature window for directly doping $LiYF_4$ NCs into TZN glass

melt is established to be between 550-625 ºC, the blue region as shown in Figure 2a. A higher temperature within the doping temperature window accelerates both the desired dispersion and the detrimental dissolution of NCs in the glass melt. To minimize the dissolution and maximize the dispersion of NCs in the glass, we examined three different doping temperatures 560 ºC, 568 ºC and 577 ºC with fixed dwell time (3 min) in preliminary experiments and found that 577 ºC is the lowest temperature enabling reasonable dispersion; at 560 ºC and 568 ºC, the viscosity of glass is too high to well disperse NCs as indicated by the presence of large aggregated NCs visible to the naked eyes.

In addition to the doping temperature, the dwell time is the other key condition for the successful direct doping of $LiYF_4$ NCs into glass. Similar to the doping temperature, prolonged dwell time aids the dispersion of NCs, but enhances the dissolution of NCs in the glass melt. To compromise the conflicting conditions in promoting dispersion and preventing dissolution of NCs, three different dwell times of 3 min, 5 min, and 10 min were investigated in preliminary experiments, which indicated the dispersion of $LiYF_4$ NCs in glass is insufficient for 3 min dwell time (as indicated by some aggregated NCs) while the NCs are totally dissolved into the glass for 10 min dwelling (as determined using analysis of fine-structure upconversion spectra of Er^{3+} detailed in Figure S9).

A modified two-temperature glass melting technique was used to prepare the UPNCs-doped TZN glass [20b]. First, a completely homogeneous and clear glass melt was obtained by melting the batch of raw materials in ambient atmosphere at 745 ºC (T_1) for 30 min. A high T_1 is used to avoid the creation of low valency tellurium species such as Te–Te bonds and low

coordinated tellurium structural units [TeO_3] that cause undesired absorption in the UV-Vis range [28]. Then, the glass melt was cooled down to 577 ºC (doping temperature T_2) and directly doped with $LiYF_4$ NCs, followed by a 5 min dwell time to disperse the doped NCs. Finally, the glass melt with dispersed NCs was cast to yield the NCs-doped TZN glass.

The Raman spectra of blank TZN glass, made by the conventional one-temperature glass melting technique, and NCs-doped TZN glass (Figure S4) show almost equal intensity for both [TeO_4] and [TeO_3] structural units. The similarity of the Raman spectra demonstrates that the glass prepared using the new two-temperature glass melting technique has the same glass network structure as the glass made by the traditional one-temperature technique. This verifies the suitability of using the two-temperature glass melting technique to maintain the glass network structure, provided that adequate melting and homogenizing of raw materials at high temperature T_1 ($\geq$ 745 ºC for melting in ambient atmosphere) are conducted.

Note that prior to doping the NCs into the TZN glass melt, the oleate ligands around $LiYF_4$ NCs were stripped off to avoid oxidation of the ligands in the glass melt. This oxidation would otherwise cause undesired scattering or absorbing defects (e.g. air bubbles or reduced tellurium species such as Te–Te bonds). The removal of the ligands by a strong acid was confirmed by FTIR spectroscopy (Figure S6) [29]. The ligand-stripped NCs were vacuum dried into a powder to ease the subsequent doping of NCs.

We doped 0.5 – 5 mg $LiYF_4$ NCs in a 30 g TZN glass melt, corresponding to approximately 17 – 170 ppm w/w. All the prepared NCs-doped TZN glasses were polished to minimize the

light scattering at surfaces (Figure S7). As illustrated in Figure 2c, the NCs-doped TZN glass samples exhibit high optical transmittance, very close to the maximum transmission of blank TZN glass from ~76.4% at 400 nm to 79.8% at 750 nm. Only a slight transmittance decrease (<5%) is observed in the 170 ppm NCs-doped TZN glass. The remarkable transmittance of the NCs-doped glasses indicates that the transparency is dominated by the multiple Fresnel reflections at the glass surface, and no significant light scattering occurred in the NCs-TZN glass.

The negligible light scattering loss is ascribed to low NCs doping concentration (≤ 170 ppm w/w), partial dissolution of doped NCs and the absence of serious agglomeration of NCs in the resulting TZN glass. For dielectric particles (such as $LiYF_4$ NCs) embedded in a homogeneous transparent medium (such as TZN glass), the extrinsic scattering coefficient (ε) is proportional to the scattering efficiency of individual particles (Q), the diameter of a particle (D), and the number of embedded particles per unit volume (N), which can be expressed [30]:

$$\varepsilon \propto Q*D^2*N \qquad (1)$$

The scattering efficiency Q is a complicated function of the particle size D, the refractive index of medium n_0, wavelength of the incident light λ and the refractive index ratio (m) of particle (n_1) to surrounding medium (n_0). In our work, the refractive index ratio of $LiYF_4$ NCs (1.4485) [31] and the host TZN glass (1.989, as given in Figure S5) at 1000 nm is m=0.73. According to the Rayleigh-Gans-Mie theory, in the case of m~0.7, particles with diameter above 600 nm lead to a constant scattering efficiency of ~2, independent of the incident light wavelength. [30] For particles with diameter below 600 nm, the scattering efficiency depends

on the particle size and presents a λ^{-4} wavelength dependence. For example, the scattering efficiency of 60 nm NCs is around two orders of magnitude lower than that of particles with diameter larger than 600 nm. As predicted by the theory, the scattering loss of 60 nm dielectric particles (m~0.7) can reduce the transmittance at 500 nm by approximately 2-3% and ~20% for 17 and 170 ppm w/w NCs-doped TZN glass (5 mm sample thickness), respectively. The transmittance decrease for 17 and 170 ppm w/w NCs-doped TZN glass relative to blank TZN glass was measured to be about 1% and 5%, respectively, which is smaller than the calculated transmission decrease. This indicates lack of NCs agglomeration in the doped TZN glass and also suggests occurrence of partial dissolution of the doped NCs. We calculated that ~50% dissolution of each NC (particles size reduction from 60 to 46 nm) leads to a transmittance drop of around 0-1% and 3-4% for 17 and 170 ppm w/w NCs-doped TZN glass, respectively.

To investigate the impact of NCs doping on the glass structure, we measured XRD patterns and Raman spectra of the blank TZN glass, and the 170 ppm NCs-doped TZN glass (0.017 wt%, which is below the XRD detection limit of ~1 wt% for crystals in a glass matrix). The absence of Bragg diffraction from crystalline lattice for the NCs-doped TZN glass reveals that the doped NCs do not induce formation of other crystals in TZN glass in quantities larger than >1% (Figure 2d). The similarity of the Raman spectra of blank TZN glass and NCs-doped TZN glass proves that the NCs-doped glass retains the original glass network structure (Figure S4). Note, nanocrystalline signatures in glass ceramics can be observed for XRD and Raman analysis because of the large amount of *in-situ* grown NCs (typical 25 – 35% volume fractions) [8a, 32].

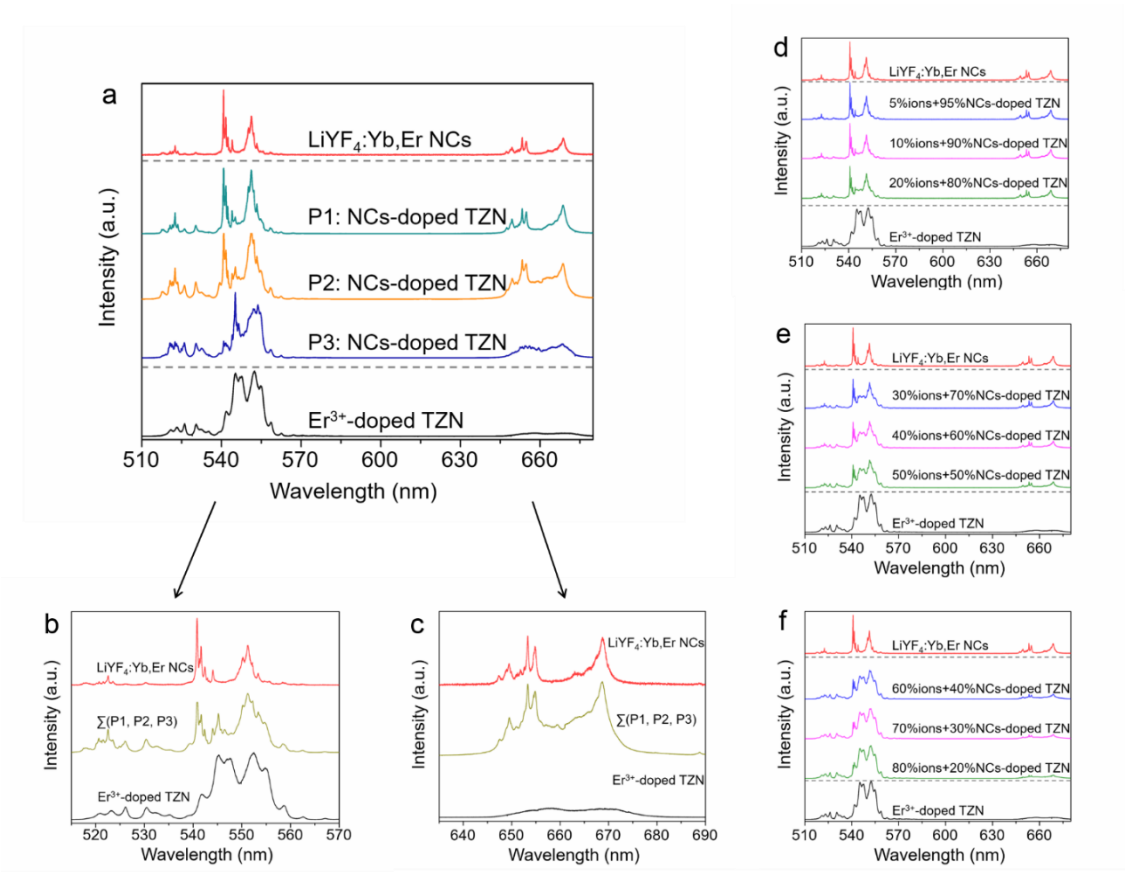

Figure 3. Upconversion spectra of as-synthesized individual $LiYF_4$:Yb,Er NCs suspension, $LiYF_4$:Yb,Er NCs-doped TZN glass and Er^{3+}-doped TZN glass. a, Normalized upconversion spectra of Er^{3+}-doped TZN glass (bottom), 170ppm NCs-doped TZN glass at different spots (middle), and NCs suspension (top). **b, c,** Zoom-in fine-structure upconversion spectra of the respective green and red emissions acquired from samples in Figure 3a, where the middle curve represents the averaged spectra of NCs-doped TZN glass at different P1, P2 and P3 spots. **d-f**, Simulated upconversion spectra by combining the emissions of Er^{3+}-doped TZN glass, and $LiYF_4$:Yb,Er NCs suspension as fractions indicated. Spectra were collected under 980 nm laser excitation (3×10^4 W/cm^2) at room temperature.

To identify the NCs survival in the TZN glass melt with a 5 min dwell at 577 ºC, we studied the fine-structure upconversion spectra of Er^{3+}-doped TZN glass, $LiYF_4$:Yb,Er NCs-doped TZN glass and $LiYF_4$:Yb,Er NCs suspension (1 mg/ml NCs in cyclohexane, which is a comparable concentration to 170 ppm NCs-doped TZN glass that equals 0.85 mg/ml NCs in glass). Under 980 nm laser excitation, all samples give Er^{3+} characteristic emissions in the green ($^2H_{11/2}$-$^4I_{15/2}$ and $^4S_{3/2}$-$^4I_{15/2}$ transitions) and red ($^4F_{9/2}$-$^4I_{15/2}$ transitions) spectral regions (energy level diagram in Figure S8) [33]. As shown in Figure 3a, the Er^{3+} ions coordinated to the glass network in the Er^{3+}-doped TZN glass exhibit inhomogeneously broadened emissions due to short-range disordered perturbations in the amorphous glass matrix [10b, 34]. By contrast, Er^{3+} ions coordinated in crystalline sites in the NCs suspension give rise to upconversion spectra with a distinct fine structure. Although the Stark splitting of Er^{3+} optical transitions occurs in both glass matrix and crystalline lattice, the Stark splitting of the continuum of different Er^{3+} coordination sites in the glass matrix smears to broad bands [23], whereas the similarity of Stark splitting of Er^{3+} ions in crystalline sites results in narrow and distinct emissions. Consequently, the existence of the same fine-structure upconversion spectra between NCs-doped TZN glasses and $LiYF_4$:Yb,Er NCs suspension demonstrates the survival of doped NCs in the TZN glass melt (Figure 3a-c, and Figure S9-different amounts of NCs in TZN glass). Moreover, the upconversion emissions in Er^{3+}-doped TZN glass show a red wavelength shift compared to the Er^{3+} ions in $LiYF_4$:Yb,Er NCs suspension (Figure 3). The red shift of optical transitions in TZN glass results from the increased degree of covalency in the bonding of Ln^{3+} ions to oxide in the TZN glass compared to the bonding to fluoride in NCs [35].

Unlike the NCs suspension and Er^{3+}-doped TZN glass that show identical upconversion spectra at varying positions within a single sample, the NCs-doped TZN glass displays upconversion spectra with diverse fine structures at different positions (recorded as P1, P2, and P3 in Figure 3a, averaged spectra in Figure 3b & 3c). We attribute this position-to-position spectral variations of NCs-doped TZN glass to the partial dissolution of doped NCs in the glass melt, which leads to a fraction of Er^{3+} ions being coordinated in the glass network instead of $LiYF_4$ crystalline lattice (these ions are hereafter referred to as glass-Er^{3+}, while the ions still in NCs are named as NCs-Er^{3+}). Therefore, the measured spectra represent a convolution of glass-related inhomogeneously broadened emissions, and crystal-related narrow emission lines (Figure 3a-c). To quantify the dissolution of doped NCs in the TZN glass melt, we simulated the upconversion spectra as a weighted combination of $LiYF_4$:Yb,Er NCs suspension spectra and Er^{3+}-doped TZN glass spectra, $S_x = xS_{ion} + (1-x)S_{NCs}$, where x is the dissolution fraction of doped NCs in the TZN glass. Comparing the measured upconversion spectra of NCs-doped TZN glass (Figure 3a-c, and Figure S9) with the simulated spectra (Figure 3d-f), the dissolution fraction of doped NCs in TZN glass lies in the region of 30% to 60%, which agrees with the dissolution rate of NCs (~50%) extracted from the transmittance calculation. The dissolution of NCs in the glass melt indicates the need for using NCs with a robust shell layer to prevent dissolution, while also allowing long dwell times for improved dispersion.

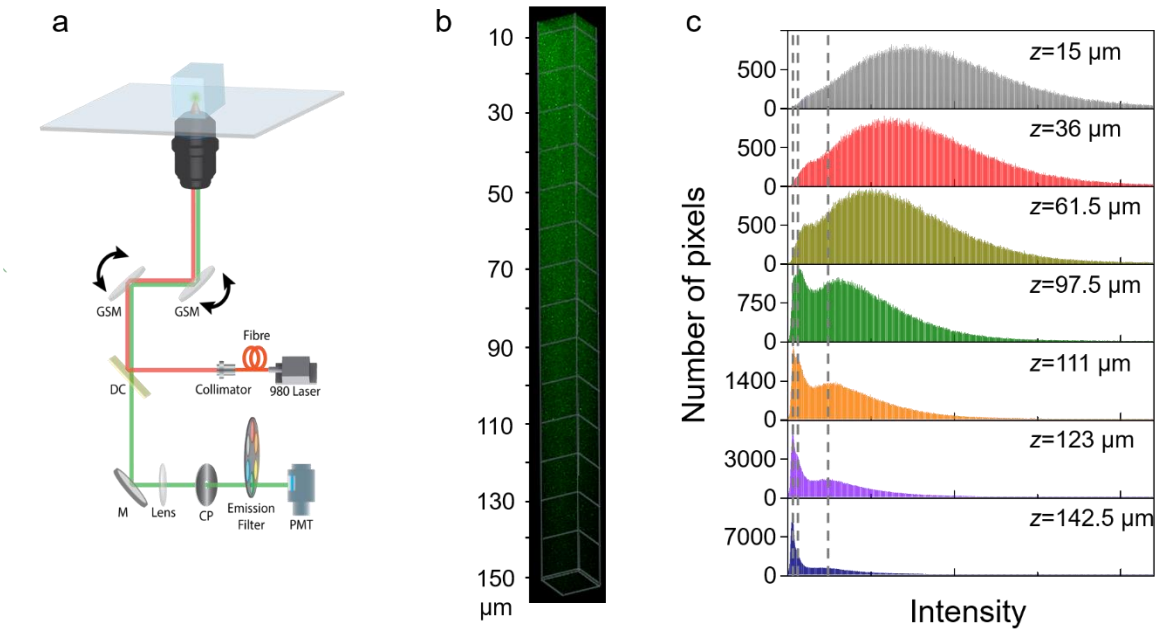

Figure 4. 3D visualization of NCs-doped TZN glass. a, Optical configuration for upconversion scanning confocal microscope. **b**, A 3D reconstruction of 67ppm NCs-doped glass by stacking 100 *x-y* planes (10 μm×10 μm square) of upconversion images at a depth (*z*) increment of 1.5 μm between the *x-y* frames. The NCs-doped glass was taken from 1 mm below the glass surface with 150 μm *z*-stack scanning. Distributed bright green dots in the image represent the detected upconversion signals: NCs are visible by high intensity dots due to large local concentration of NC-Er^{3+} ions, whereas the glass-Er^{3+} ions have lower local concentration due to NCs dissolution and diffusion of the ions into the glass matrix. The 3D image was reconstructed by IMARIS software. **c,** Histograms of upconversion intensities distribution of each pixel in the selected *x-y* frames at different depths of the *z*-stack. Top-bottom: the frame 10, 24, 41, 65, 74, 82, and 95 among 100 *x-y* planes, corresponding to depths at 15 μm, 36 μm, 61.5 μm, 97.5 μm, 111 μm, 123 μm, and 142.5 μm, respectively. The three dashed vertical lines depict the multi distribution peaks in the histogram of depth *z*=97.5μm.

To visualize the dispersion of $LiYF_4$:Yb,Er NCs in the resulting TZN glass, upconversion scanning confocal microscopy was used to scan planes within a NCs-doped TZN glass at

different depths (Figure 4a). Through reconstruction of 100 scanned *x*-*y* planes, the spatial distribution of the UPNCs in TZN glass is clearly visualized in the volumetric 3D imagery (Figure 4b). The 3D imagery element in Figure 4b shows that the NCs are unevenly distributed within a volume of 10 μm×10 μm×150 μm ($x \times y \times z$), where NCs dominantly occupy the top end and gradually decrease towards the bottom of the cuboid in this scanned unit. To shed more light on the spatial dispersion of NCs, 7 *x*-*y* planes in the 3D volumetric image at different depths (*z*-sections) were selected for analysis (4 of 7 selected planes given in Figure S10). The experimental results presented in Figure S10 suggest brighter and larger green dots in *z*=15 and 61.5 μm, in comparison to the primary fine dots in *z*=111 and 142.5 μm. To check the dispersion and dissolution of the NCs in the TZN glass, we plotted histograms of the intensity of each pixel in a *x*-*y* plane extracted from the 7 selected spatial confocal mapping images (Figure 4c). As shown in the figure, for *z*=15, 36 and 61.5 μm, one dominant intensity population with a broad and asymmetric form is observed, whereas for *z*=97.5, 111 and 123 μm three distinct intensity populations and for *z*=142.5 μm two intensity populations are observed. The illumination cone of 980 nm light in a confocal configuration has a lateral radius of approximately 523 nm. All NCs (more precisely all NCs-Er^{3+}) and all glass-Er^{3+} ions (from the partially dissolved NCs) within the excitation spot are excited and emit upconversion signal. The high intensity population band is attributed to NCs, since they have a high local concentration of Er^{3+} ions, i.e. cause high brightness per pixel. The broad width of this high intensity population band indicates varying amount of NCs per pixel, because of a large variety of NCs dispersion within the illumination cone. The low intensity population peak is attributed to glass-Er^{3+}, as the Er^{3+} ions dissolved from NCs and then diffused into the glass have lowest local Er^{3+} concentrations. The peak at the second-lowest

intensity is attributed to regions with low amount of NCs-Er^{3+} ions and/or where the glass-Er^{3+} ions have not diffused far away from the partially dissolved NCs. In the above confocal microscopy analysis, the near-infrared excitation is beneficial to remove background interference from fluorescent impurities in glass.

It is noteworthy that TEM is not a suitable methodology to characterize low concentration of NCs embedded in TZN glass (< 0.02 wt%), in particularly for the specimen prepared by grinding the glass into fine powder. Apart from the potential irradiation damage of soft tellurite glass under the high-energy electrons of TEM, locating and investigating the individual low-concentration NCs in glass is extremely challenging due to the rather small volume and very thin thickness of the specimen required for TEM characterization. By developing two optical methods with the wide field of view – 3D upconversion scanning confocal microscopy and hypersensitivity of rare earth upconversion, we not only directly provide an insight into the photonic performance of the hybrid material but also for the first time develop ways of characterizing low concentration of NCs in TZN glass over a larger scale. Both fluorescence-based methods enable representative characterizations of a larger ensemble of NCs with relative low concentrations in glass to demonstrate the survival and quantify the dissolution of doped NCs, which are hard or even impossible to be investigated by TEM.

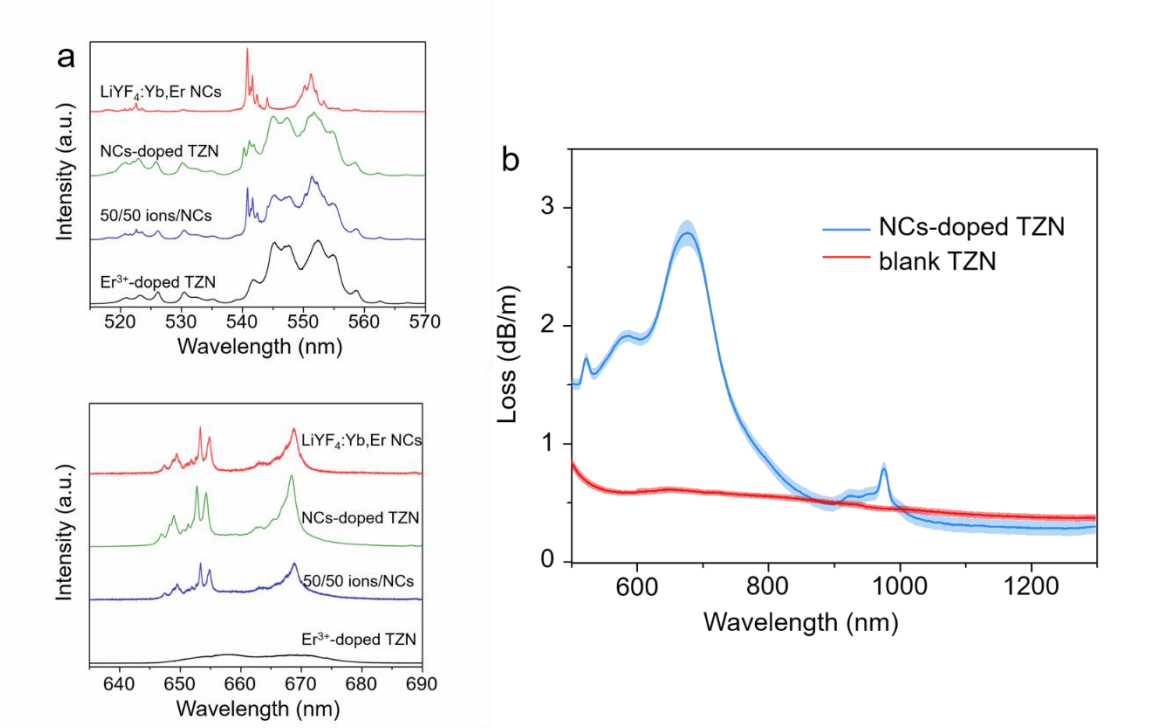

Figure 5. Optical properties of NCs-doped glass fiber. a, Normalized upconversion green (top graph) and red (bottom graph) emissions of 1mg/ml $LiYF_4$:Yb,Er NCs suspension, 70 ppm NCs-doped TZN glass fiber, simulated upconversion spectra (50/50 ions/NCs in TZN) and Er^{3+}-doped TZN glass (from top to bottom in each graph). Spectra were collected under 980 nm laser excitation (3×10^4 W/cm^2) at room temperature. **b**, Optical attenuation curve of the TZN glass fiber from 500 to 1300 nm. The blue and red curves correspond to 70 ppm NCs-doped TZN glass fiber, and blank TZN glass fiber respectively. The data are presented by means (solid curve) and range of the standard error (shaded region).

To illustrate the potential of the direct doping method to fabricate low-loss NCs-doped tellurite glass fibers, a NCs-doped TZN glass billet was extruded into a preform, and drawn into an unstructured fiber according to a previously developed protocol [36]. In Figure 5a, the fine-structure upconversion spectra of the NCs-doped glass fiber, NCs suspension and Er^{3+}-doped TZN glass suggest the dissolution fraction of NCs in the fiber remains in the range of

30%-60%, the same as in the NCs-doped glass billet. This result demonstrates no further NCs dissolution occurred during preform extrusion and fiber drawing, since the temperature used for the glass extrusion (321 ºC) and fiber drawing (~360-380 ºC) was much lower than that used for doping NCs in the glass melt (577 ºC).

The light attenuation spectrum spanning 500 nm to 1300 nm was measured to evaluate the loss of NCs-doped glass fiber. In the near-infrared region at wavelengths where Yb^{3+} ions do not absorb, the 70 ppm NCs-doped TZN glass fiber shows the same low loss as TZN fibers without NCs (Figure 5b). For example, at ~1300 nm, the NCs-doped TZN fiber exhibits a loss of 0.28±0.06 dB/m, which is between the loss of blank TZN (0.35±0.02 dB/m, Figure 5b) and Er^{3+}-doped TZN (0.08±0.06 dB/m, Figure S12) glass fibers. Using the Rayleigh-Gans-Mie theory outlined above, the scattering loss of 70 ppm of 60 nm $LiYF_4$ NCs in TZN glass at 1300 nm incident wavelength is calculated to be in the order of 10^0 dB/m, one order of magnitude higher than the measured loss of 0.3 dB/m. Taking into consideration ~50% dissolution of each NC, the calculated scattering loss is reduced to the order of 10^{-1} dB/m, which is in the same order of magnitude as the background loss of the glass itself. This result suggests that, due to the dissolution of NCs, the scattering loss becomes negligible compared to the background loss of the glass itself, confirming the occurrence of dissolution and the absence of serious agglomeration of NCs in the prepared TZN glass and fiber.

In Figure 5b, except for the absorption of Er^{3+} (peak at 523 nm) and Yb^{3+} (at 977 nm), the NCs-doped TZN glass fiber clearly exhibits absorption bands at 585 nm and 677 nm. Previous work has shown that this absorption is a consequence of the surface plasmon resonance (SPR)

of gold nanoparticles [20c]. The two peaks in our NCs-doped TZN fiber may represent the transverse and longitudinal plasmonic resonances, respectively, of rod-shaped (with length < 60 nm according to MiePlot calculation) or aggregated gold nanoparticles [37]. The formation mechanism of gold nanoparticles in TZN glass has been proposed [20b, 20c]: the corrosion of the gold crucible by the glass melt at the batch melting temperature T_1 leads to gold ions in the TZN glass, which are chemically reduced to gold atoms that grow into gold nanoparticles at lowered glass temperature (e.g., as used for the direct doping method). Furthermore, the addition of a reducing agent such as nanodiamonds is proposed to facilitate the reduction of gold ions and thus the formation of gold nanoparticles [20b]. As the SPR band of gold nanoparticles is absent in the blank TZN glass made using the same temperature program as for the NCs-doped TZN glasses, the low doping temperature T_2 used in the glass fabrication is not the reason for the presence of gold particles. One possible explanation is the residue of oleate ligands around $LiYF_4$ NCs (even after stringent acid washing – See Supplementary Information, Figure S6) could serve as a reducing agent, thereby forming gold nanoparticles. Note that the amount of such ligand residue would be below the detection limit of FTIR spectroscopy (~0.075 wt%). Another hypothetical mechanism of gold nanoparticle formation is that the $LiYF_4$ NCs serve as seeds to induce chemical reduction of gold ions and thus formation of gold particles. This possibility is supported by the presence of the SPR band in TZN glass when nanorubies were introduced in the glass melt (Figure S11). Organic ligands or impurities are excluded as nanorubies were produced *via* ball milling ruby crystals. The SPR intensity is so low (loss <3 dB/m, converted as absorption coefficient $<10^{-2}$ cm^{-1}) that it is negligible in the transmission spectra of the glass plates (<10 mm).

It is worthwhile to highlight that the direct doping method allows a highly flexible amount of NCs in glass and fiber for different applications. For NCs-doped glass fiber applications, it is practical to maintain the loss level below 10^0 dB/m to enable transmission of the signal along the fiber over a distance of meters. As outlined in the Rayleigh-Gans-Mie theory, the scattering loss of 60 nm dielectric particles with refractive index ratio m~0.7, as for UPNCs and TZN glass, is calculated to be 10^{-10} dB per particle for incident wavelength at 1300 nm in a 160 µm fiber. To keep the scattering loss below 10^0 dB/m, the number of NCs in fiber over a distance of meters is thus limited to $<10^{10}$ NCs per meter, which corresponds to <30 ppm (0.003 wt%) NCs in the TZN glass fiber (not considering any dissolution). By controlling the concentration of lanthanide-containing NCs in glass, the direct doping method enables low-loss NCs-doped fiber for fiber-based applications. For example, we propose a high-precision remote radioactivity sensor by embedding $LiYF_4:Sm^{3+}$ NCs in fiber. As Sm^{3+} are converted to Sm^{2+} under ionizing radiation, a distinct change in the fluorescence spectrum between Sm^{3+} and Sm^{2+} would enable real-time detection of radiation, e.g., inside a nuclear power station [38].

In contrast to fiber, practical applications of bulk glass, such as 3D imaging [6a] and LED lighting [19b], are tolerant to high NCs doping concentrations due to short sample length of typically less than 1 cm. Given that the scattering loss of 60 nm $LiYF_4$ NCs in TZN glass is calculated to be in the order of 0.001 dB/cm/ppm at 1000 nm and the tolerable loss of the glass is 1 dB/cm (corresponding to 79% transmittance over 1 cm optical path length excluding Fresnel reflection), ~1000 ppm (~0.1 wt%) is the upper limit of $LiYF_4$ NCs concentration in TZN bulk glass (not considering any NCs agglomeration). Higher NCs doping concentrations can be tolerated when the refractive index ratio (m) between doped NCs and the host glass is

close to 1. For example, to retain the loss of NC-doped glass below 1 dB/cm, the upper limit of embedded 60 nm NCs is 0.15 wt% (m=1.067) and 6.5 wt% (m=1.010), respectively, which is consistent with the 1-5 wt% typical NCs concentrations in glass ceramics for 3D imaging and LED lighting applications. The direct doping method is complementary to the glass ceramics not only to embed medium NCs concentrations of 0.02-1 wt% in bulk glass, but also to offer a high level of compositional and nanostructural control of NCs in glass.

3. Conclusions

In summary, we harness UPNCs and their unique properties in TZN glass and fiber *via* the direct doping method. For the first time, we quantify the dissolution fraction of $LiYF_4$ NCs in the glass by investigating the fine structure of Er^{3+} upconversion emissions, and visualize the 3D *in-situ* dispersion of UPNCs in TZN glass by upconversion scanning confocal microscopy. We demonstrate both fluorescence-based methods allow for the first time characterization of low concentration of NCs in glasses that is challenging or even impossible to be viewed under TEM. The occurrence of partial dissolution of $LiYF_4$ NCs in TZN glass (30% - 60%) suggests the need of doping NCs with a robust, sacrificial shell, e.g., SiO_2, Y_2O_3, and Al_2O_3, with much slower dissolution rate in TZN glass to prevent dissolution of the lanthanide-containing NCs core, as well as allowing long dwell times for improved dispersion of NCs in glass. Our work evidences that the direct doping method is a complementary technique of integrating NCs in a monolithic glass matrix, which offers a high level of compositional, nanostructural and doping control of Ln^{3+}-containing NCs in glass and fiber and paves the way for practical applications ranging from photonic sensor, photonic memory [38a, 38b], single photon source [20a], to microcavity lasers [6b], as well as full-color display system [6a]. In addition, the direct

doping method can be generalized to integrate other NCs with photonic, electronic and magnetic properties of interest, thus leveraging the performance and functions of the hybrid glass and fiber.

4. Experimental Section

4.1 Synthesis of $LiYF_4$:18%Yb, 4%Er nanocrystals

Reagents: Y_2O_3 (99.99%), Yb_2O_3 (99.99%), Er_2O_3 (99.99%), NaOH (98%), lithium trifluoroacetate (CF_3COOLi, 95%), trifluoroacetic acid (CF_3COOH, 99%), oleic acid (OA, 90%), and 1-octadecene (ODE, 90%) were purchased from Sigma-Aldrich and used as received without further purification.

Synthesis method: Following the protocol in literature, $LiYF_4$ nanocrystals were synthesized *via* the thermal decomposition method [39]. In a typical experiment, Y_2O_3 (108.4 mg, 0.48 mmol), Yb_2O_3 (44.3 mg, 0.112 mmol), Er_2O_3 (9.4 mg, 0.0246 mmol) were added to a 50 ml flask containing CF_3COOH (2 ml, in excess) and CF_3COOLi (180 mg, 1.5 mmol). These precursors were mixed with DI water (10 ml) and refluxed at 86 ºC for 60 minutes. OA (10 ml, in excess) and ODE (10 ml) were added, followed by degassing for 60 minutes at 110 ºC with constant stirring. The reaction was then initialized by heating the mixture to 310 ºC for 70 minutes. The resulting nanocrystals were extracted using centrifugation in 1/1 v/v MeOH/cyclohexane mixture. After repeated washing with MeOH/cyclohexane, the nanocrystals were dispersed in cyclohexane for use.

Removal of oleate ligand molecules: To yield OA ligand-free nanocrystals, the particles were thoroughly washed using 0.1 M HCl [17]. The nanocrystals were precipitated from

cyclohexane with ethanol under centrifugation. Discarding supernatant, $LiYF_4$ nanocrystals were redispersed in HCl solution and then ultrasonicated for 45 minutes to strip off the ligands from nanocrystals. The suspension was centrifuged again and further purified by washing with absolute ethanol for several times. The precipitated nanocrystals were collected before vacuum drying.

4.2 Fabrication of TZN glasses

Reagents: Glass raw materials TeO_2 (99.999%) from Suzhou Sinosun, ZnO (99.99%) and Na_2CO_3 (99.997%) from Alfa Aesar were purchased and used as received without further purification. Gold crucible was used for fabricating all glasses.

Fabrication methods: The melt-quenching technique was used to prepare TZN glass billets with composition (in mol%) $75TeO_2$-15ZnO-$10Na_2O$.

(I) For two-temperature glass melting method, the glass batch was melted in ambient atmosphere at 745 ºC (T_1) for 30 minutes. Subsequently, the glass melt temperature was reduced to 577 ºC (T_2) and maintained at 577 ºC for 10 minutes. The manual swirling was employed during T_1 and T_2 to homogenize the glass melt. For each swirling, the crucible was taken out of the muffle furnace, manually swirled for about 10 seconds, and returned to the furnace. Note that the crucible lid was removed at 577 ºC. Subsequently, dried upconversion nanocrystals with defined amount were added into the glass melt and the mixture was dwelled at 577 ºC for 5 minutes without lid; 3 minutes after doping of the nanocrystals, the melt in the crucible was mildly swirled again to further disperse doped nanocrystals. Then, the glass melt was quenched by casting into a preheated brass mould. Finally, the quenched glass was annealed for 5 hours in a muffle furnace. For this two-temperature glass melting method, the

glasses were fabricated with 30-100 g batch weight, doped with nanocrystals in the range 0-170 ppm. We prepared TZN glass without doping $LiYF_4$ NCs (referred to as blank TZN) as a control experiment.

(II) For conventional one-temperature glass melting method, the glass batch was melted (at 745 ºC for 45 minutes for blank TZN glass and at 816 ºC for 60 minutes for Yb^{3+}/Er^{3+} ions doped TZN glass), swirled, cast and annealed in ambient atmosphere. The blank glass and Er^{3+}-TZN glass was fabricated with 30 g and 100 g batch weight, respectively. We added 0.3 mg Er_2O_3 and 6 mg Yb_2O_3 to 100 g TZN batch for Er^{3+}-TZN glass.

For both two-temperature and one-temperature glass melting methods, we fabricated rectangular glass (30 g) with dimensions 15×10×30 mm^3 for spectroscopic and 3D confocal imaging analysis and cylindrical glass (100 g) with ~30 mm diameter and ~25 mm height for unstructured fiber.

4.3 Fabrication of TZN glass fiber

Preform extrusion: To make unstructured TZN glass fibers, we first extruded the 30 mm diameter cylindrical billets into 10mm diameter rod preforms using the extrusion technique [20c]. The billets were extruded by a ram at ambient atmosphere through stainless steel dies at 321 °C. The ram speed was set at 0.2 mm/min, leading to a ram force of ~3 kN in the steady-state regime of the extrusion process.

Fiber drawing: The unstructured fibers with 160 µm outer diameter were drawn from the rod preforms using a soft glass fiber drawing tower. The temperature of the tower furnace was

between 535 – 570 °C and the tower furnace was purged with mixed dry gas of 70% N_2/30% O_2 v/v.

4.4 Characterizations

General characterization: Powder X-ray diffraction (XRD) measurements were conducted on a Rigaku MiniFlex600 X-ray diffractometer from 20° to 80° (40 kV, 15 mA, Cu Kα radiation, λ = 1.5406 Å). Transmission electron microscopic (TEM) measurements were carried out on a FEI Tecnai F20 TEM operating at an acceleration voltage of 200 kV. Scanning electron microscopy (SEM) imaging was performed on a FEI Quanta 450 scanning electron microscope, at high vacuum with an accelerating voltage of 10 kV. Differential Thermal Analysis (DTA) of upconversion NCs was performed under a flowing air (20 ml min^{-1}) in a ceramic crucible on a Perkin Elmer STA8000 analyzer. All samples were dwelled at 40°C for 15 mins and ramped to 900 °C at a rate of 10°C per min. The background scan was performed under the same condition as above but without NCs. The data presented in this paper are background subtracted. Fourier transform infrared (FTIR) spectra were obtained on a Perkin Elmer FT-IR spectrometer 400, and the ranges of spectrograms were 650 to 4000 cm^{-1}. UV-Visible-NIR transmission spectra were recorded on an Agilent Cary 5000 spectrophotometer, with analysis of three random spots for the averaged spectra. The transmittance spectra measured for samples with thickness in the range of 6-8 mm were normalized to 5 mm thickness using $T_{normalized}=T_{reflection}\times(T_{measured}/T_{reflection})^{5/d}$, where $T_{reflection}$ is the transmission due to multiple Fresnel reflections (representing a maximum transmission of the sample), $T_{measured}$ is the measured transmission of sample thickness d in mm and $T_{normalized}$ is the transmission normalized to the thickness of 5 mm. The maximum transmission is

calculated using the equation $T_{reflection}=2n/(n^2+1)$, where n is the wavelength dependent refractive index, which was fitted by Sellmeier equation as described in Figure S5. Raman spectra of the polished glass pieces were acquired by Horiba Scientific LabRAM HR Evolution (1800gr/mm grating, 10× objective, 532 nm solid laser as an excitation source). The surface profiles of TZN glasses and the coverslip were characterized by a Bruker Contour GT-X.

Photoluminescence spectra: For spectroscopic measurements of NCs-doped glasses and Er^{3+}/Tm^{3+}-TZN glasses, a CW 980 nm fiber-coupled diode laser was used as the excitation source (Thorlabs BF-979-0300, 300 mW). The laser beam was reflected by a dichroic filter (Chroma T875spxrxt-UF2) and focused onto the sample by an objective (Olympus Plan N, 10×, 0.25 NA). The collected upconverting emissions was directed by the dichroic filter and coupled by a near-normal incidence short pass filter (Semrock FF01-842/SP-25), into a fiber-coupled Horiba iHR320 monochromator with CCD detector.

Upconversion scanning confocal microscopy: A confocal laser scanning microscope Olympus FV1200 equipped with a CW 980nm NIR laser was used for volumetric 3D projecting the dispersion of doped upcovnersion nanocrystals in TZN glass. The multiple-mode fiber coupled 980nm laser (Gooch and Housego; 700mW, PM fiber with FBG) was pre-aligned by a doublet collimator (F230APC-780, Thorlabs; f = 4.51 mm). The collimated excitation beam was reflected by an excitation dichroic mirror (DCM: Chroma T875spxrxt-UF2), directed by *x*/*y* galvanometer scanning mirror (GSM), and refocused onto the NCs-doped TZN glass through an objective lens (Olympus UPLFLN, 40×, 0.75 NA). The upconverted signal collected by the same objective lens passed through the DCM, confocal

pinhole (CP) and emission filter (Semrock FF01-520/70-25, for green upconversion emissions of Er^{3+}) to the PMT detector (Hamamatsu Photomultiplier R7862) in FV1200.

To generate a volumetric 3D imagery, the focused 980 nm laser beam was scanned across a defined part of the glass. By employing the software suite FV10-ASW4.1, the *x*-*y* frame was acquired in a raster pattern controlled by two high-speed oscillating mirrors driven by galvanometer motors, and *z*-depth scanning pathways of the laser beam was controlled by a motorized stepper. In our experiment, 100 *x*-*y* frames (10 μm×10 μm), taken with 1.5 μm depth increments, were stacked to yield the 3D image of the glass sample. The acquisition time of such 3D image is within 14 minutes, each *x*-*y* frame with a size of 640×640 pixels, a pixel dwell time of 20 μs. As a typical confocal scanning microscope, the illumination cone of the focused 980 nm laser beam, like a rugby ball, is determined as follows: [40]

$$\Delta x, \Delta y = 0.4\frac{\lambda}{NA} \approx 523\ nm$$

$$\Delta z = 1.4\frac{\lambda}{NA^2} \approx 2400\ nm$$

where $\Delta x = \Delta y$ is the lateral radius in *x*-*y*, Δz is the elongated radius along the *z*-axis, and λ is the excitation wavelength 980 nm. In this manner, multi upconversion nanocrystals in the illumination cone are excited simultaneously and emit upconversion signal when scanning.

Fiber loss: The fiber loss spectra in the range of 500 to 1300 nm were measured using the cutback technique with a tungsten filament bulb as the light source. The broadband light was collimated and focused into the fiber, and then the output signal was launched into an optical spectrum analyzer (OSA). We performed more than 4 cutbacks for each fiber, with 3 cleaves for each cutback length to minimize the measurement error.

Corresponding Author

* Correspondence and requests for materials should be addressed to J.Z. and H.E. tim.zhao@adelaide.edu.au and heike.ebendorff@adelaide.edu.au

Acknowledgement

This work has been supported by ARC grant DP130102494 and CE140100003. This work was performed in part at the OptoFab node of the Australian National Fabrication Facility utilizing Commonwealth and SA State Government funding. PI and TLN acknowledged the Melbourne Materials Institute for the Interdisciplinary Seed Funding Grant. We thank support from Hong Ji and Alastair Dowler for glass and fiber preparation and from Herbert Foo, Jingrun Ran, and Abel Santos for sample characterization.

Supporting Information Available: Supporting Figures S1–12. The Supporting Information is available free of charge from the Wiley Online library or from the author.

REFERENCES

1. (a) Zhao, J.; Jin, D.; Schartner, E. P.; Lu, Y.; Liu, Y.; Zvyagin, A. V.; Zhang, L.; Dawes, J. M.; Xi, P.; Piper, J. A.; Goldys, E. M.; Monro, T. M., Single-nanocrystal sensitivity achieved by enhanced upconversion luminescence. *Nat Nano* **2013,** *8* (10), 729-734; (b) Gargas, D. J.; Chan, E. M.; Ostrowski, A. D.; Aloni, S.; Altoe, M. V. P.; Barnard, E. S.; Sanii, B.; Urban, J. J.; Milliron, D. J.; Cohen, B. E.; Schuck, P. J., Engineering bright sub-10-nm upconverting nanocrystals for single-molecule imaging. *Nat Nano* **2014,** *9* (4), 300-305; (c)

Zhou, J.; Chen, G.; Zhu, Y.; Huo, L.; Mao, W.; Zou, D.; Sun, X.; Wu, E.; Zeng, H.; Zhang, J., Intense multiphoton upconversion of Yb 3+–Tm 3+ doped β-NaYF 4 individual nanocrystals by saturation excitation. *Journal of Materials Chemistry C* **2015,** *3* (2), 364-369.

2. Wang, J.; Deng, R.; MacDonald, M. A.; Chen, B.; Yuan, J.; Wang, F.; Chi, D.; Andy Hor, T. S.; Zhang, P.; Liu, G.; Han, Y.; Liu, X., Enhancing multiphoton upconversion through energy clustering at sublattice level. *Nat Mater* **2014,** *13* (2), 157-162.

3. (a) Chen, X.; Peng, D.; Ju, Q.; Wang, F., Photon upconversion in core–shell nanoparticles. *Chemical Society Reviews* **2015,** *44* (6), 1318-1330; (b) Li, X.; Zhang, F.; Zhao, D., Lab on upconversion nanoparticles: optical properties and applications engineering via designed nanostructure. *Chemical Society Reviews* **2015,** *44* (6), 1346-1378.

4. Liu, D.; Xu, X.; Du, Y.; Qin, X.; Zhang, Y.; Ma, C.; Wen, S.; Ren, W.; Goldys, E. M.; Piper, J. A., Three-dimensional controlled growth of monodisperse sub-50 [thinsp] nm heterogeneous nanocrystals. *Nature communications* **2016,** *7*.

5. (a) Zhou, B.; Shi, B.; Jin, D.; Liu, X., Controlling upconversion nanocrystals for emerging applications. *Nature nanotechnology* **2015,** *10* (11), 924-936; (b) Dong, H.; Du, S.-R.; Zheng, X.-Y.; Lyu, G.-M.; Sun, L.-D.; Li, L.-D.; Zhang, P.-Z.; Zhang, C.; Yan, C.-H., Lanthanide Nanoparticles: From Design toward Bioimaging and Therapy. *Chemical Reviews* **2015,** *115* (19), 10725-10815.

6. (a) Deng, R.; Qin, F.; Chen, R.; Huang, W.; Hong, M.; Liu, X., Temporal full-colour tuning through non-steady-state upconversion. *Nat Nano* **2015,** *10* (3), 237-242; (b) Zhu, H.; Chen, X.; Jin, L. M.; Wang, Q. J.; Wang, F.; Yu, S. F., Amplified Spontaneous Emission and Lasing from Lanthanide-Doped Up-Conversion Nanocrystals. *Acs Nano* **2013,** *7* (12), 11420-11426.

7. (a) Dejneka, M. J., Transparent oxyfluoride glass ceramics. *Mrs Bulletin* **1998,** *23* (11), 57-62; (b) Herrmann, A.; Tylkowski, M.; Bocker, C.; Rüssel, C., Cubic and Hexagonal NaGdF4 Crystals Precipitated from an Aluminosilicate Glass: Preparation and Luminescence Properties. *Chemistry of Materials* **2013,** *25* (14), 2878-2884.

8. (a) Xiaoying, S.; Ping, C.; Wenjing, C.; Kan, Z.; Jing, M.; Donghai, F.; Shian, Z.; Zhenrong, S.; Jianrong, Q.; Tianqing, J., Fine tunable red-green upconversion luminescence from glass ceramic containing 5%Er 3+:NaYF 4 nanocrystals under excitation of two near infrared femtosecond lasers. *Journal of Applied Physics* **2014,** *116* (6), 063101 (8 pp.)-063101 (8 pp.); (b) Melekhin, V. G.; Kolobkova, E. V.; Lipovskii, A. A.; Petrikov, V. D.; Malyarevich, A. M.; Savitsky, V. G., Fluorophosphate glasses doped with PbSe quantum dots and their nonlinear optical characteristics. *Glass Physics and Chemistry* **2008,** *34* (4), 351-355; (c) Masai, H.; Fujiwara, T.; Takahashi, Y., *Glass-Ceramics Containing Nano-Crystallites of Oxide Semiconductor*. INTECH Open Access Publisher: 2010; (d) Mattarelli, M.; Gasperi, G.; Montagna, M.; Verrocchio, P., Transparency and long-ranged fluctuations: The case of glass ceramics. *Physical Review B* **2010,** *82* (9), 094204.

9. (a) Ledemi, Y.; Trudel, A.-A.; Rivera, V. A. G.; Chenu, S.; Veron, E.; Nunes, L. A.; Allix, M.; Messaddeq, Y., White light and multicolor emission tuning in triply doped Yb3+/Tm3+/Er3+ novel fluoro-phosphate transparent glass-ceramics. *Journal of Materials Chemistry C* **2014,** *2* (25), 5046-5056; (b) Wang, Y.; Ohwaki, J., New transparent vitroceramics codoped with Er3+ and Yb3+ for efficient frequency upconversion. *Applied Physics Letters* **1993,** *63* (24), 3268-3270; (c) Chen, D.; Wang, Y.; Yu, Y.; Huang, P.; Weng, F., Near-infrared quantum cutting in transparent nanostructured glass ceramics. *Optics letters* **2008,** *33* (16), 1884-1886.

10. (a) Jha, A.; Richards, B.; Jose, G.; Teddy-Fernandez, T.; Joshi, P.; Jiang, X.; Lousteau, J., Rare-earth ion doped TeO2 and GeO2 glasses as laser materials. *Progress in Materials Science* **2012,** *57* (8), 1426-1491; (b) Jha, A.; Shen, S.; Naftaly, M., Structural origin of spectral broadening of 1.5-mu m emission in Er3+-doped tellurite glasses. *Physical Review B* **2000,** *62* (10), 6215-6227; (c) Gao, G.; Winterstein-Beckmann, A.; Surzhenko, O.; Dubs, C.; Dellith, J.; Schmidt, M. A.; Wondraczek, L., Faraday rotation and photoluminescence in heavily Tb3+-doped GeO2-B2O3-Al2O3-Ga2O3 glasses for fiber-integrated magneto-optics. *Sci. Rep.* **2015,** *5*.

11. (a) Jiang, N.; Zhou, S.; Su, D.; Qiu, J., Do Eu dopants prefer the precipitated LaF3 nanocrystals in glass ceramics? *physica status solidi (RRL)-Rapid Research Letters* **2012,** *6* (12), 487-489; (b) de Pablos-Martin, A.; Patzig, C.; Höche, T.; Duran, A.; Pascual, M., Distribution of thulium in Tm3+-doped oxyfluoride glasses and glass-ceramics. *CrystEngComm* **2013,** *15* (35), 6979-6985; (c) de Pablos-Martín, A.; García, M. A.; Muñoz-Noval, A.; Castro, G. R.; Pascual, M. J.; Durán, A., Analysis of the distribution of Tm3 + ions in LaF3 containing transparent glass-ceramics through X-ray absorption spectroscopy. *Journal of Non-Crystalline Solids* **2014,** *384*, 83-87.

12. (a) Tick, P. A.; Borrelli, N. F.; Cornelius, L. K.; Newhouse, M. A., Transparent glass ceramics for 1300 nm amplifier applications. *Journal of Applied Physics* **1995,** *78* (11), 6367-6374; (b) Hendy, S., Light scattering in transparent glass ceramics. *Applied Physics Letters* **2002,** *81* (7), 1171-1173.

13. (a) Dong, H.; Sun, L.-D.; Wang, Y.-F.; Ke, J.; Si, R.; Xiao, J.-W.; Lyu, G.-M.; Shi, S.; Yan, C.-H., Efficient Tailoring of Upconversion Selectivity by Engineering Local Structure of Lanthanides in NaxREF3+x Nanocrystals. *Journal of the American Chemical Society* **2015,**

137 (20), 6569-6576; (b) Zhang, Y.; Zhang, L.; Deng, R.; Tian, J.; Zong, Y.; Jin, D.; Liu, X., Multicolor Barcoding in a Single Upconversion Crystal. *Journal of the American Chemical Society* **2014,** *136* (13), 4893-4896.

14. Liu, C.; Heo, J., Lead Chalcogenide Quantum Dot-Doped Glasses for Photonic Devices. *International Journal of Applied Glass Science* **2013,** *4* (3), 163-173.

15. Souza, N. M.; Ramos, A. Y.; Barbosa, L. C., Er3+ environment in TeO2–ZnO–Na2O glasses. *Journal of Non-Crystalline Solids* **2002,** *304* (1–3), 195-199.

16. Munasinghe, H. T.; Winterstein-Beckmann, A.; Schiele, C.; Manzani, D.; Wondraczek, L.; Afshar V, S.; Monro, T. M.; Ebendorff-Heidepriem, H., Lead-germanate glasses and fibers: a practical alternative to tellurite for nonlinearfiber applications. *Optical Materials Express* **2013,** *3* (9), 1488-1503.

17. Wang, F.; Deng, R.; Wang, J.; Wang, Q.; Han, Y.; Zhu, H.; Chen, X.; Liu, X., Tuning upconversion through energy migration in core–shell nanoparticles. *Nat Mater* **2011,** *10* (12), 968-973.

18. (a) Gajc, M.; Surma, H. B.; Klos, A.; Sadecka, K.; Orlinski, K.; Nikolaenko, A. E.; Zdunek, K.; Pawlak, D. A., Nanoparticle Direct Doping: Novel Method for Manufacturing Three-Dimensional Bulk Plasmonic Nanocomposites. *Advanced Functional Materials* **2013,** *23* (27), 3443-3451; (b) Karaksina, E. V.; Shiryaev, V. S.; Ketkova, L. A., Preparation of composite materials for fiber optics based on chalcogenide glasses containing ZnS(ZnSe):Cr(2+) crystals. *Journal of Non-Crystalline Solids* **2013,** *377*, 220-224.

19. (a) Zhou, Y.; Chen, D.; Tian, W.; Ji, Z., Impact of Eu3+ Dopants on Optical Spectroscopy of Ce3+: Y3Al5O12 ‐ Embedded Transparent Glass ‐ Ceramics. *Journal of the American Ceramic Society* **2015**; (b) Huang, J.; Hu, X.; Shen, J.; Wu, D.; Yin, C.; Xiang, R.;

Yang, C.; Liang, X.; Xiang, W., Facile synthesis of a thermally stable Ce 3+: Y 3 Al 5 O 12 phosphor-in-glass for white LEDs. *CrystEngComm* **2015,** *17* (37), 7079-7085; (c) Chai, G.; Dong, G.; Qiu, J.; Zhang, Q.; Yang, Z., 2.7 μm Emission from Transparent Er3+,Tm3+ Codoped Yttrium Aluminum Garnet (Y3Al5O12) Nanocrystals–Tellurate Glass Composites by Novel Comelting Technology. *The Journal of Physical Chemistry C* **2012,** *116* (37), 19941-19950.

20. (a) Henderson, M. R.; Gibson, B. C.; Ebendorff-Heidepriem, H.; Kuan, K.; Afshar V, S.; Orwa, J. O.; Aharonovich, I.; Tomljenovic-Hanic, S.; Greentree, A. D.; Prawer, S.; Monro, T. M., Diamond in Tellurite Glass: a New Medium for Quantum Information. *Advanced Materials* **2011,** *23* (25), 2806-2810; (b) Ebendorff-Heidepriem, H.; Ruan, Y.; Ji, H.; Greentree, A. D.; Gibson, B. C.; Monro, T. M., Nanodiamond in tellurite glass Part I: origin of loss in nanodiamond-doped glass. *Optical Materials Express* **2014,** *4* (12), 2608-2620; (c) Ruan, Y.; Ji, H.; Johnson, B. C.; Ohshima, T.; Greentree, A. D.; Gibson, B. C.; Monro, T. M.; Ebendorff-Heidepriem, H., Nanodiamond in tellurite glass Part II: practical nanodiamond-doped fibers. *Optical Materials Express* **2015,** *5* (1), 73-87.

21. (a) Malinowski, M.; Joubert, M.; Jacquier, B., Dynamics of the IR-to-blue wavelength upconversion in Pr 3+-doped yttrium aluminum garnet and LiYF 4 crystals. *Physical Review B* **1994,** *50* (17), 12367; (b) Chen, G.; Ohulchanskyy, T. Y.; Kachynski, A.; Ågren, H.; Prasad, P. N., Intense visible and near-infrared upconversion photoluminescence in colloidal LiYF4: Er3+ nanocrystals under excitation at 1490 nm. *ACS nano* **2011,** *5* (6), 4981-4986.

22. Kim, S. Y.; Won, Y.-H.; Jang, H. S., A Strategy to enhance Eu3+ emission from LiYF4:Eu nanophosphors and green-to-orange multicolor tunable, transparent nanophosphor-polymer composites. *Scientific Reports* **2015,** *5*, 7866.

23. Jørgensen, C. K.; Judd, B., Hypersensitive pseudoquadrupole transitions in lanthanides. *Molecular Physics* **1964,** *8* (3), 281-290.

24. Dong, A.; Ye, X.; Chen, J.; Kang, Y.; Gordon, T.; Kikkawa, J. M.; Murray, C. B., A Generalized Ligand-Exchange Strategy Enabling Sequential Surface Functionalization of Colloidal Nanocrystals. *Journal of the American Chemical Society* **2011,** *133* (4), 998-1006.

25. (a) Oermann, M. R.; Ebendorff-Heidepriem, H.; Li, Y.; Foo, T.-C.; Monro, T. M., Index matching between passive and active tellurite glasses for use in microstructured fiber lasers: Erbium doped lanthanum-tellurite glass. *Optics express* **2009,** *17* (18), 15578-15584; (b) Manning, S.; Ebendorff-Heidepriem, H.; Monro, T. M., Ternary tellurite glasses for the fabrication of nonlinear optical fibres. *Optical Materials Express* **2012,** *2* (2), 140-152.

26. (a) Thoma, R.; Weaver, C.; Friedman, H.; Insley, H.; Harris, L.; Yakel Jr, H., Phase equilibria in the system LiF—YF3. *The Journal of Physical Chemistry* **1961,** *65* (7), 1096-1099; (b) Maier, D.; Bertram, R.; Klimm, D.; Fornari, R., Influence of the atmosphere on the growth of LiYF4 single crystal fibers by the micro‐pulling‐down method. *Crystal Research and Technology* **2009,** *44* (2), 137-140.

27. Da, N.; Wondraczek, L.; Schmidt, M. A.; Granzow, N.; Russell, P. S. J., High index-contrast all-solid photonic crystal fibers by pressure-assisted melt infiltration of silica matrices. *Journal of Non-Crystalline Solids* **2010,** *356* (35–36), 1829-1836.

28. Ogbuu, O.; Du, Q.; Lin, H.; Li, L.; Zou, Y.; Koontz, E.; Smith, C.; Danto, S.; Richardson, K.; Hu, J., Impact of Stoichiometry on Structural and Optical Properties of Sputter Deposited Multicomponent Tellurite Glass Films. *Journal of the American Ceramic Society* **2015**.

29. Bogdan, N.; Vetrone, F.; Ozin, G. A.; Capobianco, J. A., Synthesis of ligand-free colloidally stable water dispersible brightly luminescent lanthanide-doped upconverting nanoparticles. *Nano letters* **2011,** *11* (2), 835-840.

30. France, P., *Fluoride glass optical fibres*. Springer Science & Business Media: 2012.

31. Castleberry, D. E.; Linz, A., Measurement of the refractive indices of LiYF 4. *Appl. Opt.* **1975,** *14* (9), 2056_1-2056.

32. (a) Chenu, S.; Véron, E.; Genevois, C.; Garcia, A.; Matzen, G.; Allix, M., Long-lasting luminescent ZnGa 2 O 4: Cr 3+ transparent glass-ceramics. *Journal of Materials Chemistry C* **2014,** *2* (46), 10002-10010; (b) Gonçalves, M. C.; Santos, L. F.; Almeida, R. M., Rare-earth-doped transparent glass ceramics. *Comptes Rendus Chimie* **2002,** *5* (12), 845-854.

33. Zhao, J.; Lu, Z.; Yin, Y.; McRae, C.; Piper, J. A.; Dawes, J. M.; Jin, D.; Goldys, E. M., Upconversion luminescence with tunable lifetime in NaYF 4: Yb, Er nanocrystals: role of nanocrystal size. *Nanoscale* **2013,** *5* (3), 944-952.

34. Hehlen, M. P.; Cockroft, N. J.; Gosnell, T. R.; Bruce, A. J., Spectroscopic properties of Er3+- and Yb3+-doped soda-lime silicate and aluminosilicate glasses. *Physical Review B* **1997,** *56* (15), 9302-9318.

35. Jackson, S. D., Towards high-power mid-infrared emission from a fibre laser. *Nat Photon* **2012,** *6* (7), 423-431.

36. Ebendorff-Heidepriem, H.; Kuan, K.; Oermann, M. R.; Knight, K.; Monro, T. M., Extruded tellurite glass and fibers with low OH content for mid-infrared applications. *Optical Materials Express* **2012,** *2* (4), 432-442.

37. Juluri, B. K.; Lu, M.; Zheng, Y. B.; Huang, T. J.; Jensen, L., Coupling between Molecular and Plasmonic Resonances: Effect of Molecular Absorbance. *The Journal of Physical Chemistry C* **2009,** *113* (43), 18499-18503.

38. (a) Riesen, N.; François, A.; Badek, K.; Monro, T. M.; Riesen, H., Photoreduction of Sm3+ in Nanocrystalline BaFCl. *The Journal of Physical Chemistry A* **2015,** *119* (24), 6252-6256; (b) Ramana Reddy, M. V.; Gopal Reddy, C.; Narasimha Reddy, K., Thermoluminescence characteristics of Sm3+ doped NaYF4 crystals. *Bulletin of Materials Science* **2007,** *30* (1), 1-3; (c) Wells, J.-P. R.; Sugiyama, A.; Han, T. P. J.; Gallagher, H. G., A spectroscopic comparison of samarium-doped LiYF4 and KY3F10. *Journal of Luminescence* **2000,** *87–89*, 1029-1031.

39. Mahalingam, V.; Vetrone, F.; Naccache, R.; Speghini, A.; Capobianco, J. A., Colloidal Tm3+/Yb3+-Doped LiYF4 Nanocrystals: Multiple Luminescence Spanning the UV to NIR Regions via Low-Energy Excitation. *Advanced Materials* **2009,** *21* (40), 4025-4028.

40. Pawley, J. B., Fundamental limits in confocal microscopy. In *Handbook of biological confocal microscopy*, Springer: 2006; pp 20-42.

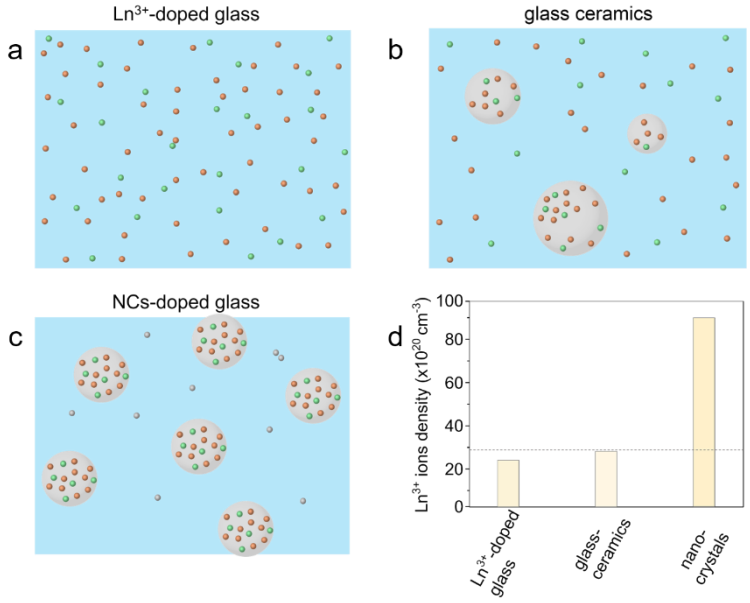

Figure 1. Schematic diagram of Ln^{3+} distribution in various glasses. a, glass containing Ln^{3+} ions (Ln^{3+}-doped glass), **b,** glass containing *in-situ* grown NCs (glass ceramics), **c,** glass with directly doped NCs (NCs-doped glass). The small grey dots represent the Ln^{3+} ions in NCs-doped glass that were formed by dissolution of NCs, which could be prevented by using NCs with a robust shell. **d**, Schematic of Ln^{3+} ion densities available in glasses, NCs in glass ceramics, and as-synthesized individual NCs, indicating that up to 23×10^{20} Ln^{3+}/cm^3, and 28×10^{20} Ln^{3+}/cm^3 have been achieved in glasses and glass ceramics respectively, whereas up to 90×10^{20} Ln^{3+}/cm^3 is feasible in individual NCs synthesized in solvents. It is reported that up to ~10×10^{20} Ln^{3+}/cm^3 was doped in tellurite glass or ZBLAN glass [15], and up to 23×10^{20} Ln^{3+} ions/cm^3 was achieved in germanate glass [16]. The Ln^{3+} ions density of *in-situ* grown NCs in glass ceramics is slightly higher than that of Ln^{3+}-doped glass, since the Ln^{3+} ions in the glass are diffused and concentrated in the grown NCs. However, the relatively small diffusion of Ln^{3+} ions into the grown NCs (considerable residual Ln^{3+} in the glass matrix), and large volume fractions of these NCs in glass limit the maximum concentration of Ln^{3+} ions in grown NCs. For instance, a doping level of 28×10^{20} Ln^{3+}/cm^3 was obtained when 30% of the total Ln^{3+} ions diffuse from the glass into *in-situ* grown NCs [11c], and 25% volume fraction of the grown NCs (NCs/glass vol/vol) occupy the glass [12]. In contrast, wet chemistry synthesis of NCs, where the ionic radius of the cationic sites in crystalline matrix is close to that of Ln^{3+} ions, permits the cationic sites to

be completely occupied by Ln^{3+} ions. This enables considerably higher Ln^{3+} ion densities in as-synthesized NCs [1a, 17], and hence in such NCs-doped glass.

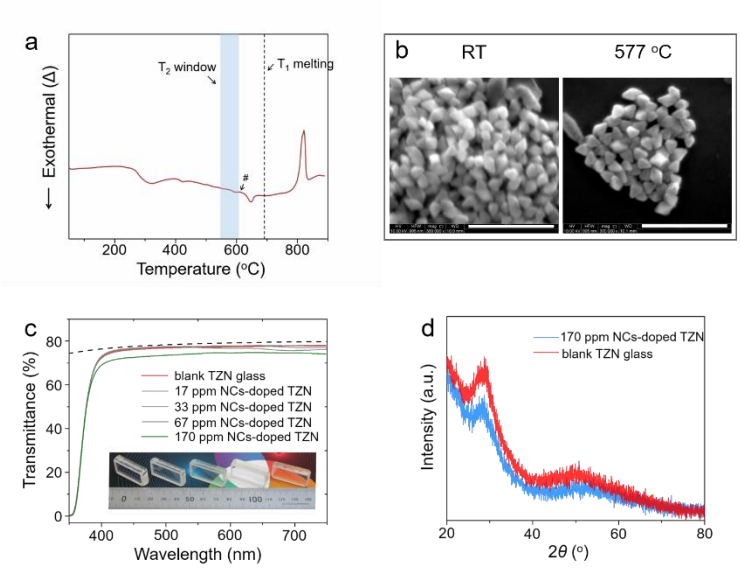

Figure 2. General characterizations of $LiYF_4$ NCs and NCs-doped TZN glasses. a, DTA analysis of $LiYF_4$ NCs to determine the decomposition temperature. The blue band represents the T_2 temperature window suitable for directly doping $LiYF_4$ NCs in TZN glass melt. The vertical dashed line is the batch melting temperature T_1 used for preparing TZN glass. The exothermic signal between 300 ºC and 450 ºC is ascribed to the oxidation of the original oleate ligands around $LiYF_4$ NCs. [24] **b,** SEM images of $LiYF_4$ NCs before (left column) and after (right column) annealing at 577 ºC for 5 min. $LiYF_4$ NCs was spiked on a glass coverslip for this test. Scale bar: 500 nm. **c,** Transmittance spectra of bulk TZN glasses doped with varying amounts of $LiYF_4$ NCs. The solid curves represent the averaged transmission spectra of three different spots of each glass and are normalized to a glass thickness of 5 mm as described in the supplement. The top dashed line is the calculated transmittance for TZN glass taking into account multiple Fresnel reflections at the sample surfaces as described in Figure S5 [25]. The exponential drop of the measured transmission results from the electronic band gap absorption of TZN glass. The bottom inset is an optical photograph of blank and NCs-doped TZN

glasses, left → right: blank TZN glass, ~ 17, 33, 67, and 170 ppm $LiYF_4$ NCs-doped TZN glasses. All samples are colourless and transparent. **d**. XRD spectra of blank and NCs-doped TZN glass, showing only the broad bands of amorphous glass and no crystalline footprint.

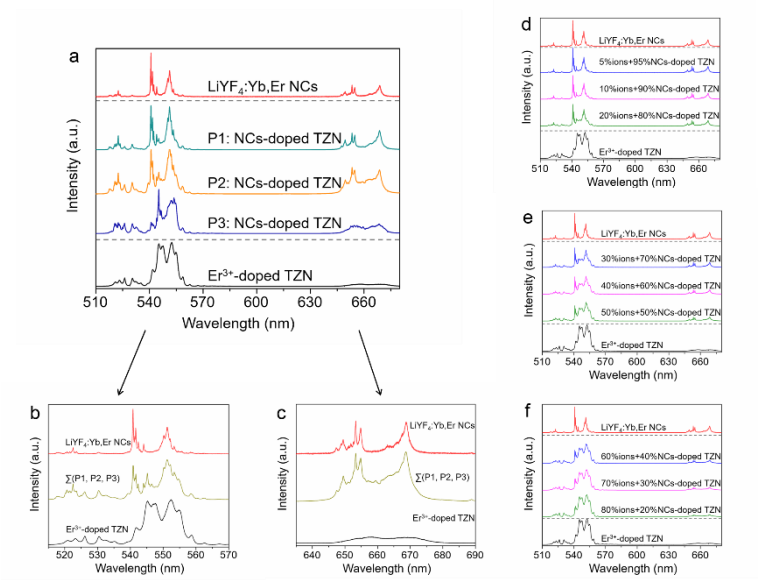

Figure 3. Upconversion spectra of as-synthesized individual $LiYF_4$:Yb,Er NCs suspension, $LiYF_4$:Yb,Er NCs-doped TZN glass and Er^{3+}-doped TZN glass. a, Normalized upconversion spectra of Er^{3+}-doped TZN glass (bottom), 170ppm NCs-doped TZN glass at different spots (middle), and NCs suspension (top). **b, c,** Zoom-in fine-structure upconversion spectra of the respective green and red emissions acquired from samples in Figure 3a, where the middle curve represents the averaged spectra of NCs-doped TZN glass at different P1, P2 and P3 spots. **d-f**, Simulated upconversion spectra by combining the emissions of Er^{3+}-doped TZN glass, and $LiYF_4$:Yb,Er NCs suspension as fractions indicated. Spectra were collected under 980 nm laser excitation (3×10^4 W/cm^2) at room temperature.

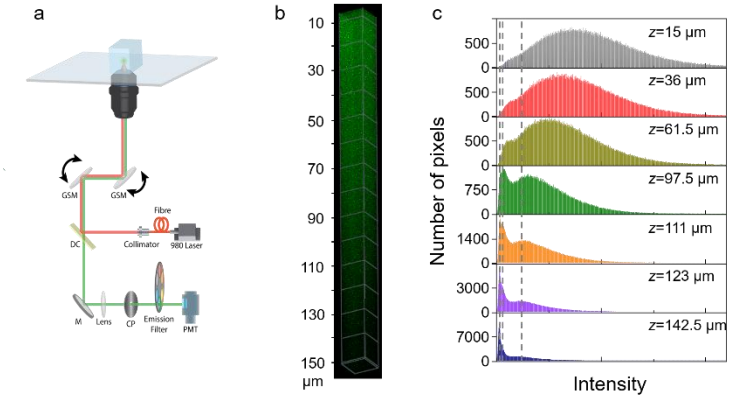

Figure 4. 3D visualization of NCs-doped TZN glass. a, Optical configuration for upconversion scanning confocal microscope. **b**, A 3D reconstruction of 67ppm NCs-doped glass by stacking 100 *x-y* planes (10 μm×10 μm square) of upconversion images at a depth (*z*) increment of 1.5 μm between the *x-y* frames. The NCs-doped glass was taken from 1 mm below the glass surface with 150 μm *z*-stack scanning. Distributed bright green dots in the image represent the detected upconversion signals: NCs are visible by high intensity dots due to large local concentration of NC-Er^{3+} ions, whereas the glass-Er^{3+} ions have lower local concentration due to NCs dissolution and diffusion of the ions into the glass matrix. The 3D image was reconstructed by IMARIS software. **c,** Histograms of upconversion intensities distribution of each pixel in the selected *x-y* frames at different depths of the *z*-stack. Top-bottom: the frame 10, 24, 41, 65, 74, 82, and 95 among 100 *x-y* planes, corresponding to depths at 15 μm, 36 μm, 61.5 μm, 97.5 μm, 111 μm, 123 μm, and 142.5 μm, respectively. The three dashed vertical lines depict the multi distribution peaks in the histogram of depth *z*=97.5μm.

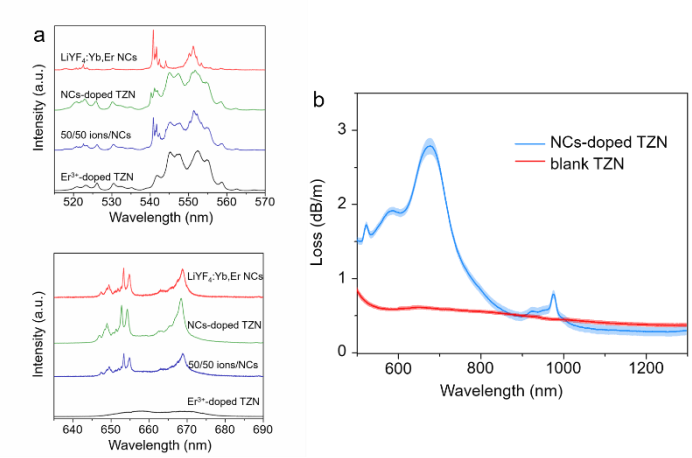

Figure 5. Optical properties of NCs-doped glass fiber. a, Normalized upconversion green (top graph) and red (bottom graph) emissions of 1mg/ml $LiYF_4$:Yb,Er NCs suspension, 70 ppm NCs-doped TZN glass fiber, simulated upconversion spectra (50/50 ions/NCs in TZN) and Er^{3+}-doped TZN glass (from top to bottom in each graph). Spectra were collected under 980 nm laser excitation (3×10^4 W/cm^2) at room temperature. **b**, Optical attenuation curve of the TZN glass fiber from 500 to 1300 nm. The blue and red curves correspond to 70 ppm NCs-doped TZN glass fiber, and blank TZN glass fiber respectively. The data are presented by means (solid curve) and range of the standard error (shaded region).

Supplementary Information

Upconversion nanocrystals doped glass: a new paradigm for photonic materials

Jiangbo Zhao[1,4], Xianlin Zheng[2,4], Erik P. Schartner[1,4], Paul Ionescu[3], Run Zhang[1], Tich-Lam Nguyen[3], Dayong Jin[2,4,5], Heike Ebendorff-Heidepriem[1,4*]*

[1] Institute of Photonics and Advanced Sensing and School of Chemistry and Physics, University of Adelaide, Adelaide, SA 5005, Australia

[2] Advanced Cytometry Laboratories, MQ Biofocus Research Centre, Macquarie University, Sydney, NSW 2109, Australia

[3] Bio21 Institute and School of Chemistry, University of Melbourne, Melbourne, VIC 3010, Australia

[4] ARC Centre of Excellence for Nanoscale BioPhotonics

[5] Institute for Biomedical Materials and Devices, Faculty of Science, University of Technology Sydney, NSW, 2007, Australia

[*] Correspondence and requests for materials should be addressed to J.Z. and H.E. tim.zhao@adelaide.edu.au and heike.ebendorff@adelaide.edu.au,

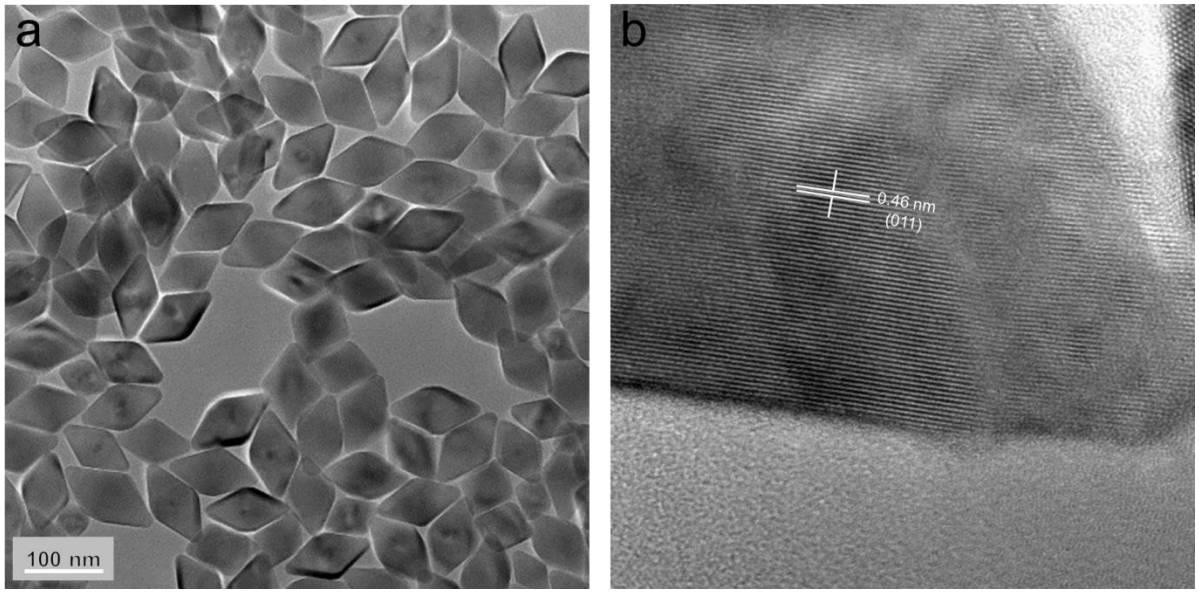

Figure S1. (a) TEM image of the as-prepared $LiYF_4$ nanocrystals. (b) High-resolution TEM image of a nanocrystal reveals its highly crystalline nature with lattice fringe *d*-spacing of 0.46 nm, well matched to the lattice distance in the [011] plane of tetragonal-phase $LiYF_4$.

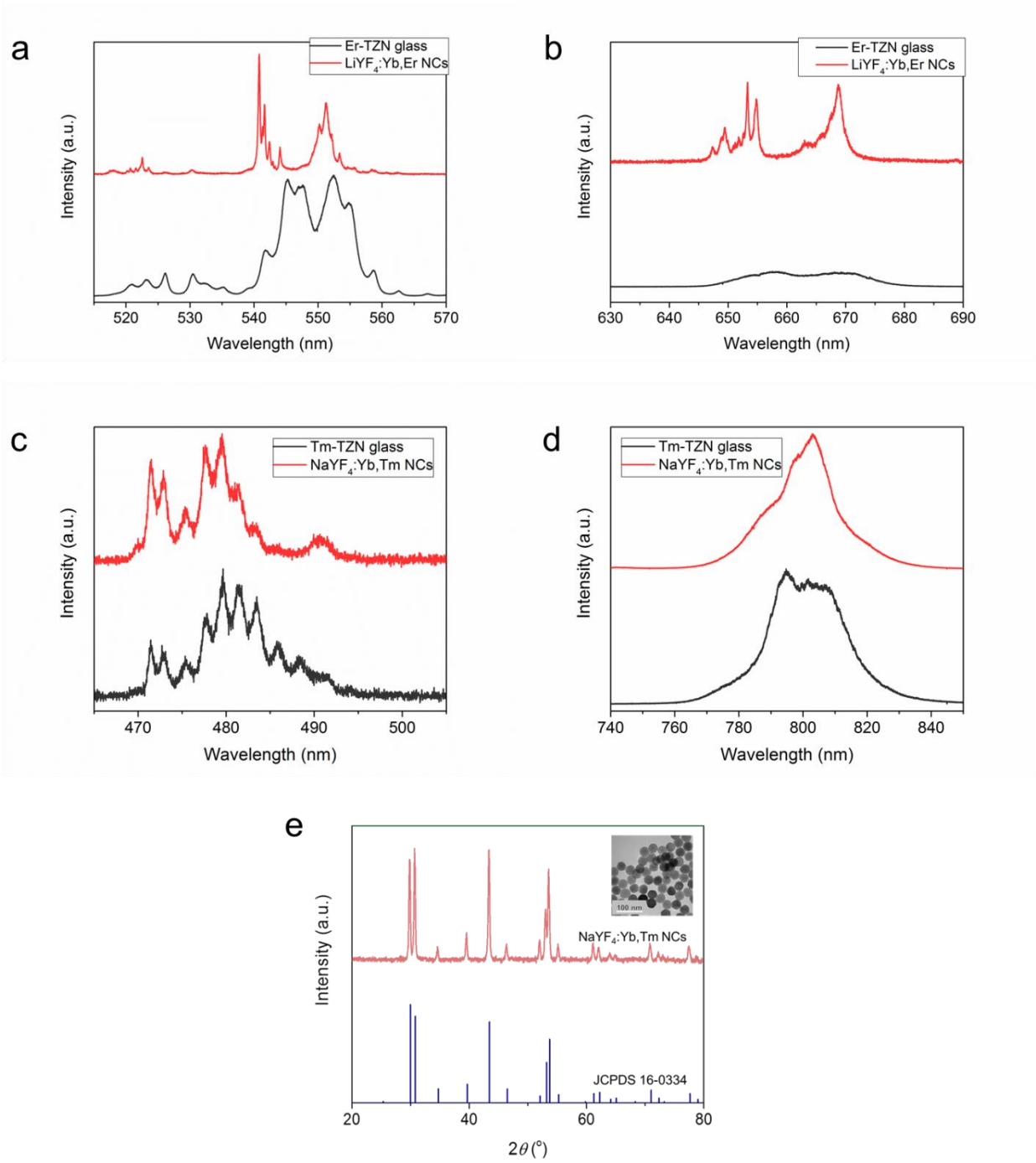

Figure S2. (a-d), Fine-structure upconversion emissions of Er^{3+} and Tm^{3+} in amorphous and nanocrystalline matrixes, respectively, demonstrating the high sensitivity of Er^{3+} emissions to the surroundings. The energy levels involved in those upconversion luminescence are given in Fig. S8. (d) Powder XRD patterns of $NaYF_4$:Yb,Tm NCs are in agreement with JCPDS 16-0334 (hexagonal phase). Powder XRD patterns of $LiYF_4$:Yb,Er NCs can be referred to Fig. S3. Inset: TEM image of $NaYF_4$:Yb,Tm NCs.

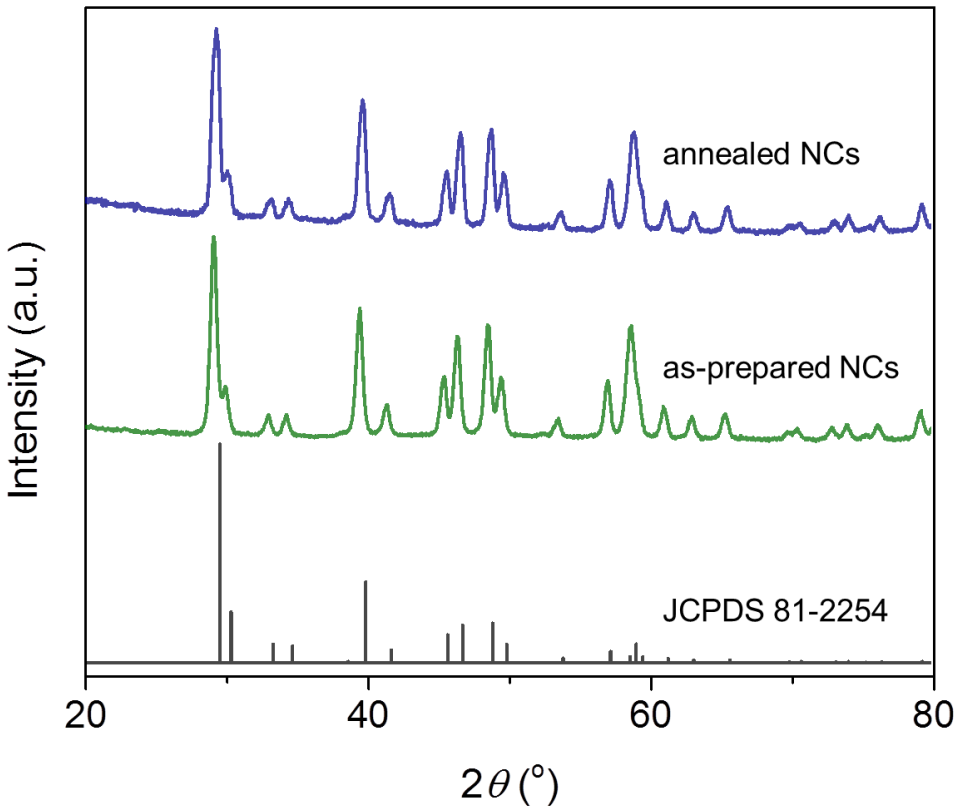

Figure S3. Powder XRD patterns of annealed $LiYF_4$ NCs (top, 577 °C for 5 mins) and as-synthesized $LiYF_4$ NCs (middle). The diffraction peaks which are well indexed to JCPDS 81-2254 (bottom tetragonal phase $LiYF_4$) confirm the crystalline stability of NCs with a moderate heating for certain time.

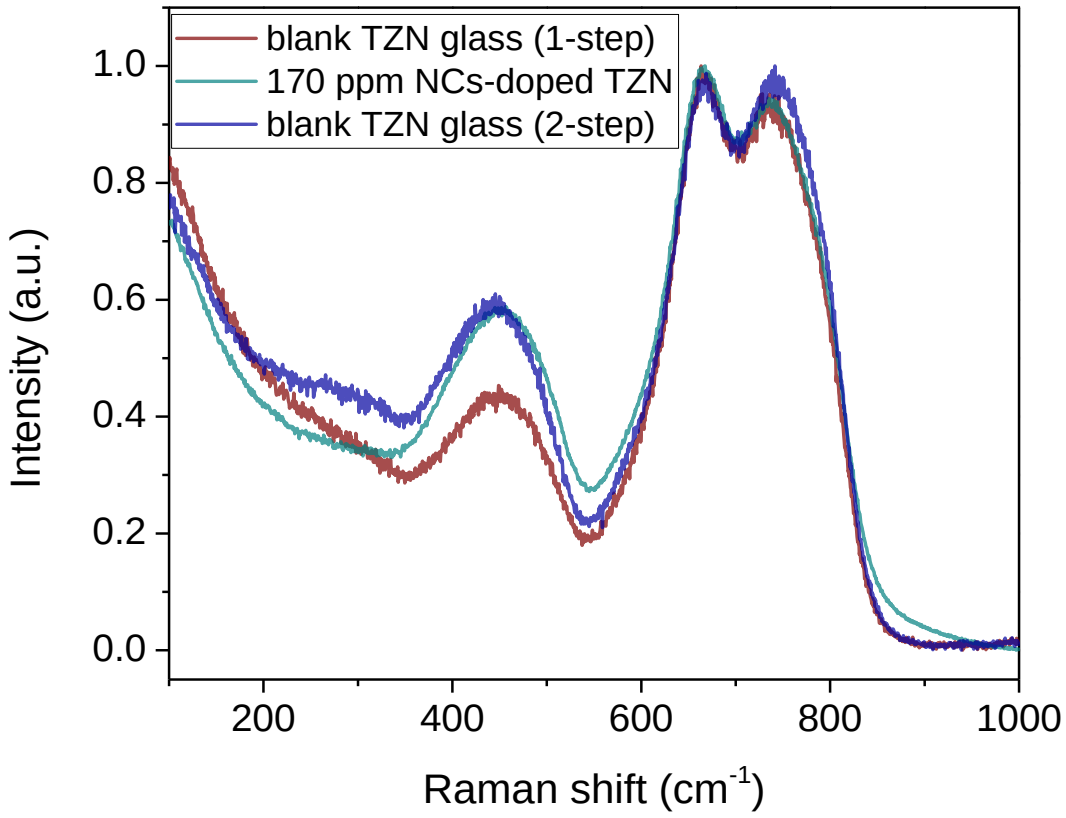

Figure S4. Raman spectra of blank TZN glasses made by one-temperature (1-step) and two-temperature (2-step) glass melting technique, respectively, and NCs-doped TZN glass prepared using the direct doping method with two-temperature step. The figure shows all Raman spectra are dominated by intense and broad bands at around 740 cm^{-1} and 665 cm^{-1}. The 740 cm^{-1} band is contributed by stretching of Te–O or Te=O which contain non-bridging oxygen in [TeO_3] or [$TeO_{3+\delta}$] structural units, while the band at around 665 cm^{-1} originates from asymmetric stretching vibrations of Te–O in [TeO_4] structural units with bridging oxygen. The relatively weak but broad scattering peak at around 420 cm^{-1} is assigned to the bending and stretching vibrations of Te–O–Te or O–Te–O linkages in between two [TeO_4] sharing corner sites. [1,2]

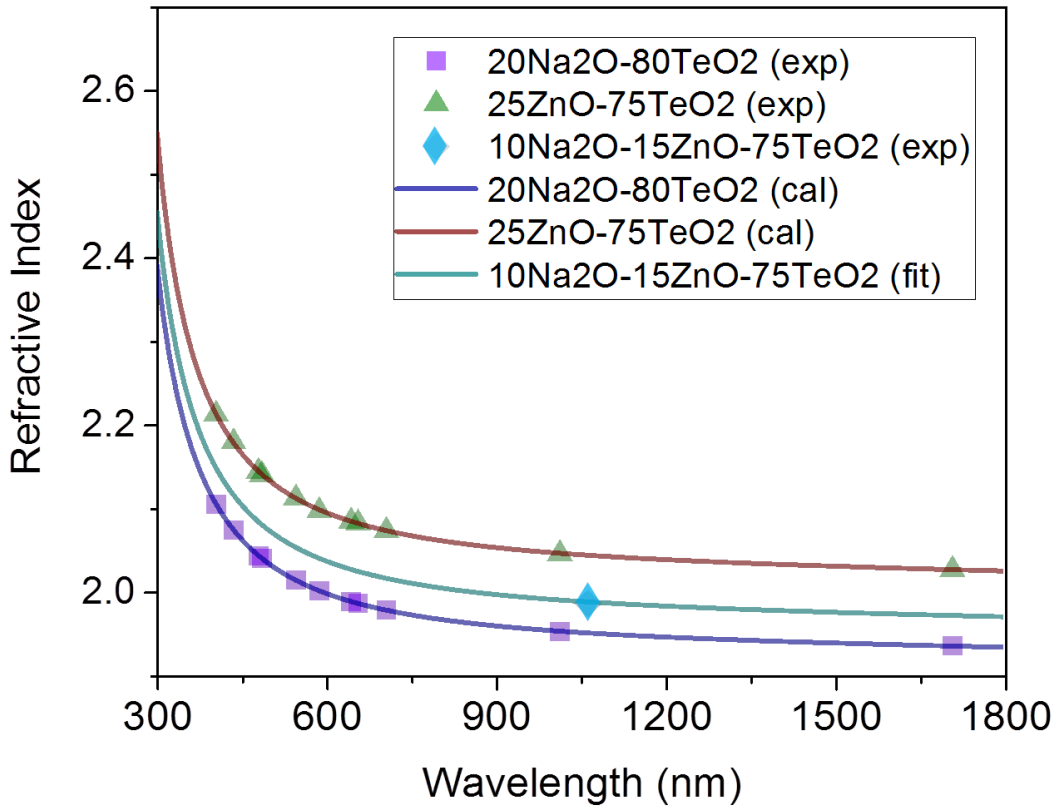

Figure S5. Refractive index versus wavelength for tellurite-based glasses, including $20Na_2O$-$80TeO_2$, $25ZnO$-$75TeO_2$, and $10Na_2O$-$15ZnO$-$75TeO_2$. Solid square, triangle and diamond points are experimental values with accuracy of $\pm 2.0\times10^{-4}$ to $\pm 5.0\times10^{-5}$. [3,4] The curves of $20Na_2O$-$80TeO_2$ and $25ZnO$-$75TeO_2$ are simulated according to Sellmeier equation: $n^2=A+B(1-C/\lambda^2)+D/(1-E/\lambda^2)$, where A, B, C, D, and E constants for $20Na_2O$-$80TeO_2$, are A=2.1810511, B=1.5538234, C=5.0408437×10^{-2}, D=1.9356580, and E=225, and for $25ZnO$-$75TeO_2$, are A= 2.4843245, B= 1.6174321, C= 5.3715551×10^{-2}, D= 2.4765135, and E=225, respectively. Because of the lack of constants for $10Na_2O$-$15ZnO$-$75TeO_2$, the refractive index curve of this glass was plotted by weighting the $20Na_2O$-$80TeO_2$ and $25ZnO$-$75TeO_2$ glasses with the respective factor 0.6 and 0.4 to best fit the reported experiment point (solid diamond).

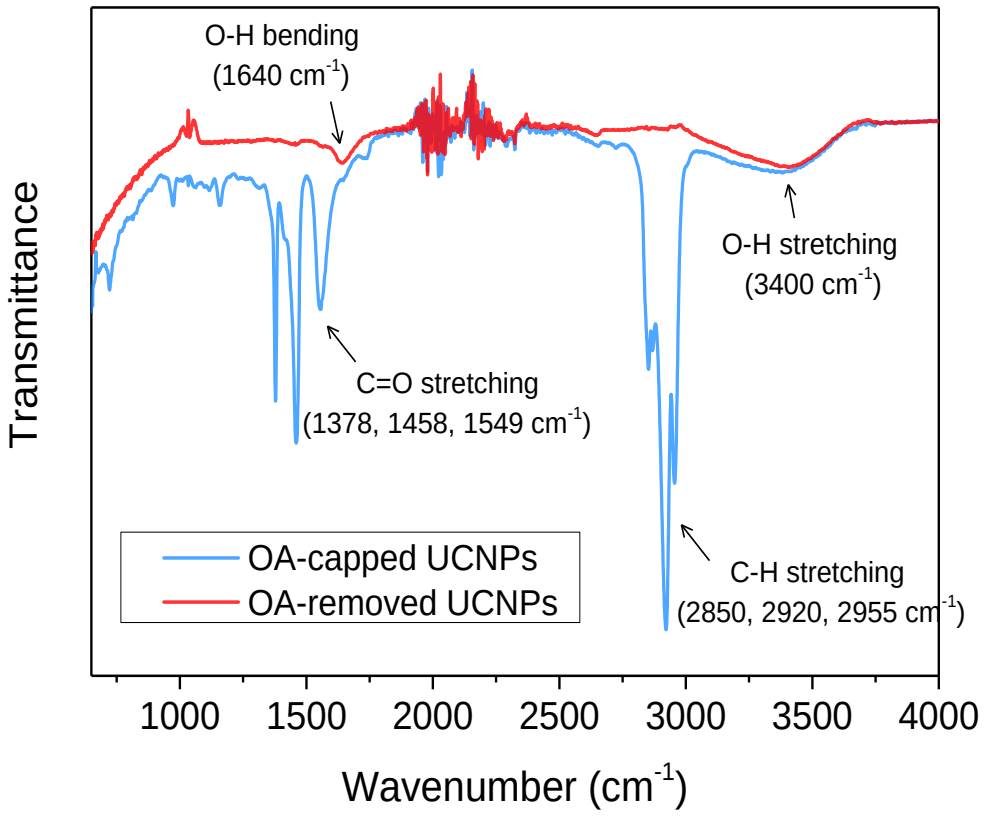

Figure S6. FTIR spectra of $LiYF_4$ NCs treated by HCl solution confirm the removal of OA ligands. After HCl processing, the C-H and C=O stretching vibrations which are associated with original oleate ligands become negligible. Note the detection limit of FTIR is reported above 0.075 wt%. [5]

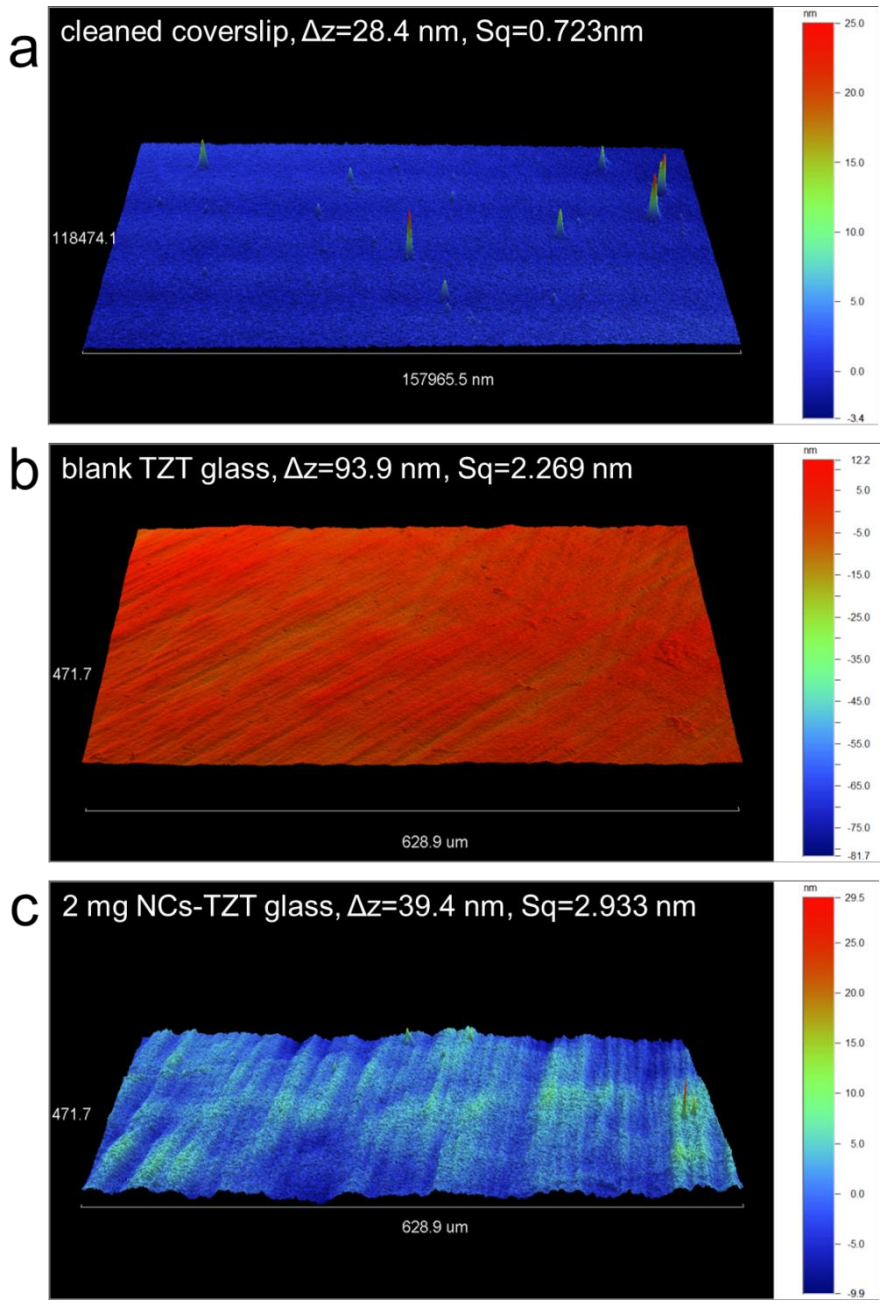

Figure S7. Optical profiler images of (a) a cleaned commercial coverslip, (b) blank TZN glass, and (c) NCs-doped TZN glass, indicating the high quality surface of as-fabricated glasses which are comparable to the commercial coverslip. All images are displayed with different lateral scale, denoted as Δz. The degree of surface roughness of each glass is given by the average Sq value, extracted from the profilometer data.

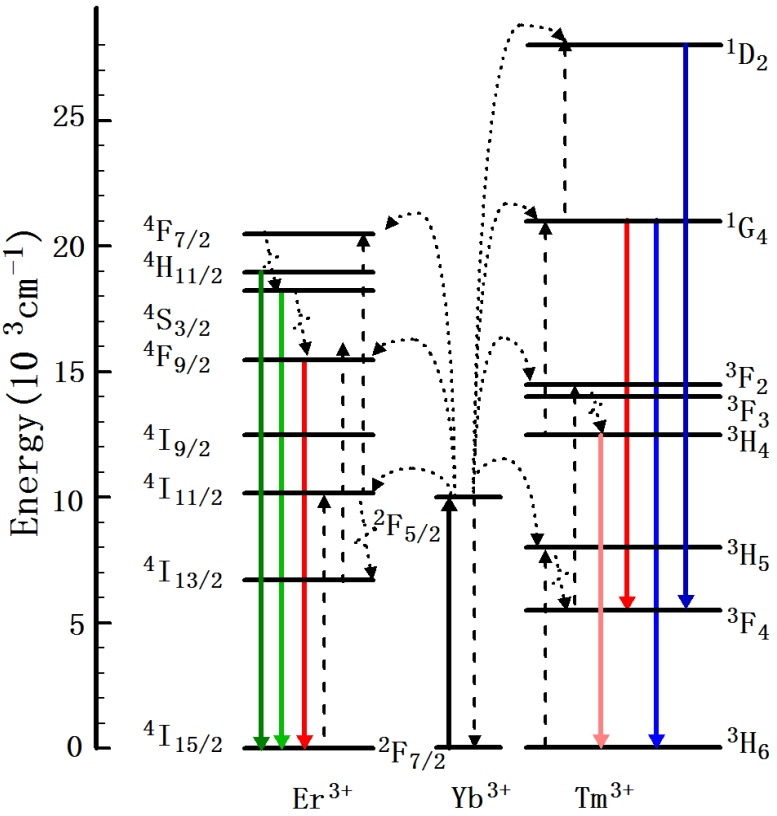

Figure S8. Simplified scheme of upconversion luminescence in Yb-Er and Yb-Tm pairs. Black solid arrow: infrared photon absorption; black dashed arrows: energy transfer processes; and colour solid arrows: upconversion emissions. The spectroscopic notation $^{2S+1}L_J$ associated with the respective energy levels represents the spin (*S*), orbital (*L*) and total angular (*J*) momentum quantum numbers in Ln^{3+}.

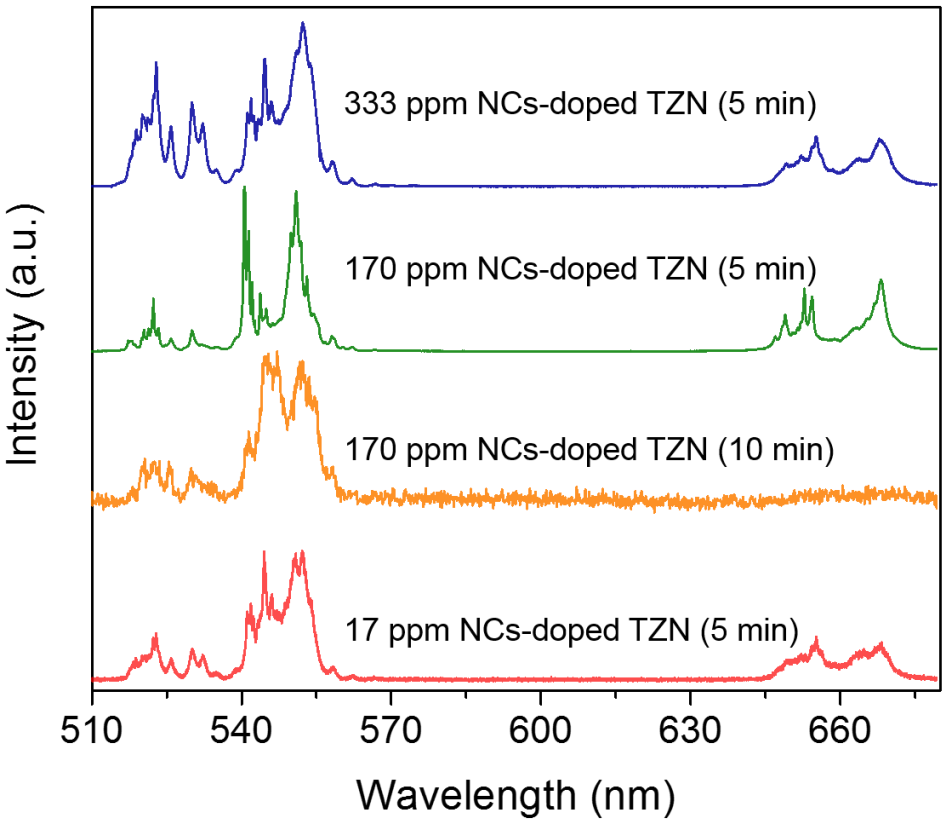

Figure S9. Upconversion spectra of TZN glasses doped with different amounts of $LiYF_4$:Yb,Er NCs with varying dwell time.

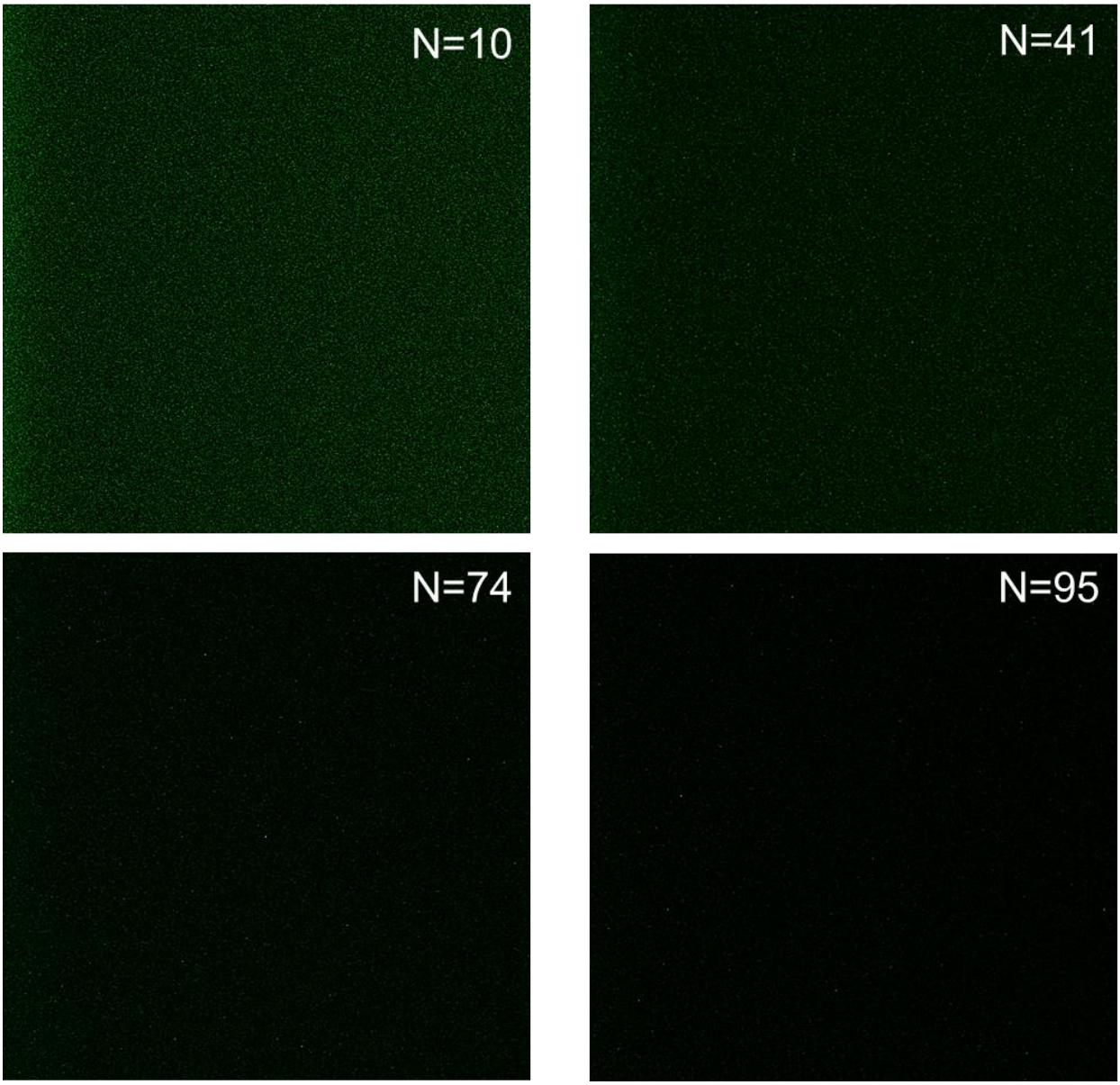

Fig. S10. Confocal mapping of 4 selected x-y frames at different depths from the z-stack, showing a typical dispersion of NCs in the resulting TZN glass. The distributed green dots in the optical sections represent the detected upconversion signals. Each frame is 10 μm×10 μm square. N means the number of layers among 100 stacking planes.

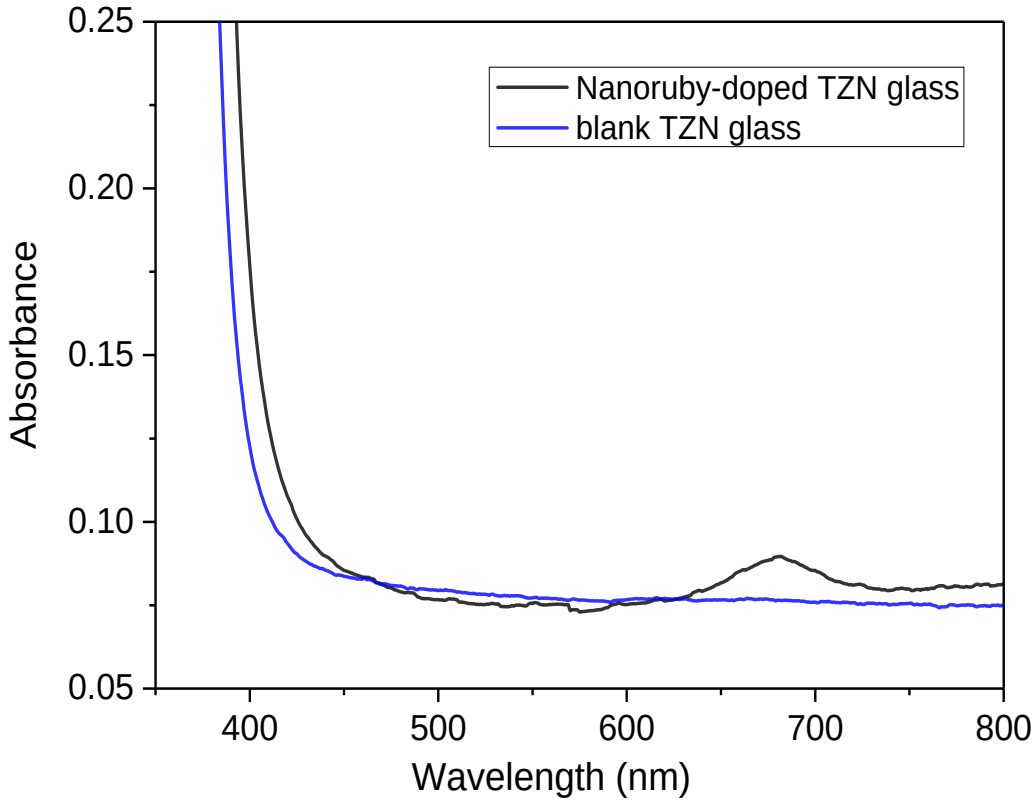

Figure S11. Absorption spectra of nanoruby-doped TZN glass show the appearance of SPR band peak at 681 nm, while the curve of blank TZN glass is flat.

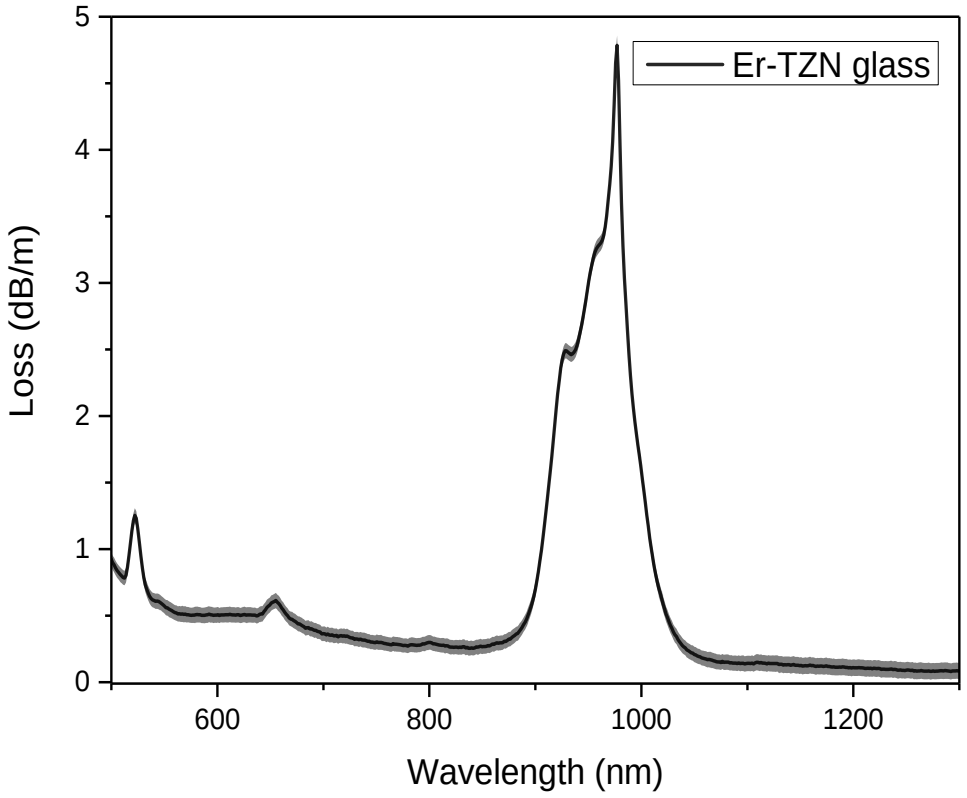

Figure S12. Fibre loss spectrum of Er-TZN glass presented by means (solid black curve) and range of the standard error (shaded grey region) over wavelength from 500 nm to 1300 nm.

References

1 Jha, A., Shen, S. & Naftaly, M. Structural origin of spectral broadening of 1.5-mu m emission in Er3+-doped tellurite glasses. *Physical Review B* **62**, 6215-6227 (2000).

2 Zhang, A. D., Lin, A. X., Wang, J. S. & Toulouse, J. Multistage etching process for microscopically smooth tellurite glass surfaces in optical fibers. *Journal of Vacuum Science & Technology B* **28**, 682-686 (2010).

3 Manning, S., Ebendorff-Heidepriem, H. & Monro, T. M. Ternary tellurite glasses for the fabrication of nonlinear optical fibres. *Optical Materials Express* **2**, 140-152 (2012).

4 Ghosh, G. Sellmeier Coefficients and Chromatic Dispersions for Some Tellurite Glasses. *Journal of the American Ceramic Society* **78**, 2828-2830 (1995).

5 Chan, K. L. A. & Kazarian, S. G. Detection of trace materials with Fourier transform infrared spectroscopy using a multi-channel detector. *Analyst* **131**, 126-131 (2006).